Computing Smooth and Integrable Cross Fields via Iterative Singularity Adjustment

Long Ma, Ying He, *Member, IEEE*, Jianmin Zheng, Yuanfeng Zhou, Shiqing Xin, Caiming Zhang, and Wenping Wang, *Fellow, IEEE*

***Abstract*—We propose a new method for computing smooth and integrable cross fields on 2D and 3D surfaces. our approach first computes smooth cross fields by minimizing the Dirichlet energy. Unlike existing optimization-based methods, our technique determines the singularity configuration–i.e., the number, locations, and indices of singularities–by iteratively adjusting them. Singularities can move, merge and split, akin to the behavior of like charges repelling and unlike charges attracting. Once all singularities stop moving, we obtain a cross field with (locally) the lowest Dirichlet energy. In simply connected domains, this cross field is guaranteed to be integrable. However, this property does not hold in multiply connected domains. To make a smooth cross field integrable, we construct a vector field c that characterizes the deviation of the cross field from a curl-free field. We then optimize the locations of singularities by moving them along the field lines of c. Our method is fundamentally different from existing integer programming-based approaches, as it avoids combinatorial optimization. It is fully automatic and includes a parameter to control the number of singularities. Our method is well suited for smooth models where exact boundary alignment and sparse hard directional constraints are desired, and can guide seamless conformal parameterization and T-junction-free quadrangulation.**

***Index Terms*—Cross field, dirichlet energy, integrability, iterative singularity adjustment, singularity placement.**

I. Introduction

A CROSS field, also known as a 4-RoSy field [1], [2], is a directional field that exhibits rotational symmetry and is invariant under rotations of $\frac{\pi}{2}$ radians. Originally introduced by Hertzmann and Zorin as a computational tool for non-photorealistic cross-hatching rendering [3], cross fields have gained significant prominence in the construction of high-quality quadrilateral meshes [4], [5]. These meshes are highly desired in various engineering fields, including simulation [6] and finite element analysis [7].

Constrained by the topology of the surface on which it is defined, a cross field cannot possess an arbitrary arrangement of singularities. If the singularities of the cross field are predetermined, including their number, placement, and indices, smooth cross fields can be generated directly by solving a sparse linear system [8]. The computation of smooth cross fields with unknown singularities is commonly formulated as an optimization problem, and numerous methods exist for solving it [4], [9], [10], [11], [12].

Cross fields are commonly utilized as a guidance in the computation of global conformal parameterization, from which quadrilateral meshes can be extracted. A cross field is *integrable* if it aligns well with the gradient of some scalar field on the surface. When the computed cross fields are integrable, the parameterization can be obtained directly by tracing the integral curves of the cross fields. However, for non-integrable cross fields, it is necessary to compute a pair of parameters (u, v) by minimizing the difference between the gradients of the parameters and the directions of the cross fields. In cases where the integrability of the cross fields is poor, the resulting parameterization may be misaligned with the desired cross field and can even exhibit inversions [13].

It is well known that in simply connected domains, a smooth cross field, which has the minimal Dirichlet energy, is guaranteed to be integrable [14]. Unfortunately, this desirable property does not extend to multiply connected domains, where the non-trivial topology imposes significant constrains on the solution space for achieving both smoothness and integrability in cross fields.

Existing research efforts have primarily concentrated on computing smooth cross fields with optimal singularities, with relatively less attention given to the issue of integrability. Only a few attempts have been made to explicitly address the integrability problem by relaxing either the orthogonality [13], [15] or the equal length constraints [16] of the cross fields, thereby expanding the solution space. To the best of our knowledge, *there is currently no research that addresses both the smoothness and integrability of cross fields on surfaces with arbitrary topology.*

This paper aims to investigate the relationship between the smoothness and integrability of cross fields defined on smooth

Manuscript received 4 February 2024; revised 1 June 2024; accepted 7 June 2024. Date of publication 25 June 2024; date of current version 1 August 2025. This work was supported in part by the Ministry of Education, Singapore, under its Academic Research Fund under Grant MOE-T2EP20220-0005, Grant RT19/22, and Grant RG12/22, in part by the National Natural Science Foundations of China under Grant 62172257 and Grant 62272277, and in part by the Fundamental Research Funds of Shandong University under Grant 11480061. Recommended for acceptance by Y. Tong. *(Corresponding authors: Ying He; Yuanfeng Zhou.)*

Long Ma, Yuanfeng Zhou, and Caiming Zhang are with the School of Software, Shandong University, Jinan 250100, China (e-mail: malong@sdu.edu.cn; yfzhou@sdu.edu.cn).

Ying He and Jianmin Zheng are with the College of Computing and Data Science, Nanyang Technological University, Singapore 639798 (e-mail: yhe@ntu.edu.sg; asjmzheng@ntu.edu.sg).

Shiqing Xin is with the School of Computer Science, Shandong University, Jinan 250100, China.

Wenping Wang is with the Department of Computer Science & Engineering, Texas A&M University, College Station, TX 77843 USA.

Source code is available at https://github.com/GSW-D/Cross-Field.

This article has supplementary downloadable material available at https://doi.org/10.1109/TVCG.2024.3418892, provided by the authors.

Digital Object Identifier 10.1109/TVCG.2024.3418892

(a) Initial random cross field θ_0 (b) Smooth cross field θ_1 (c) Smooth & integrable field θ_2 (d) Induced parameterization (u, v)

Fig. 1. We develop an automatic method for computing smooth and integrable cross fields on 3D surfaces of complex topology. The algorithm takes as input a random cross field with 4,341 positive (red) and 4,397 negative (blue) singularities (a). It first smooths the cross field by iteratively adjusting singularities. When two singularities of opposite indices meet, they annihilate, resulting in a drop in the Dirichlet energy. When all singularities stop moving, the Dirichlet energy reaches a local minimum. The resulting cross field is smooth and has only 85 positive and 141 negative singularities (b). However, this cross field is not integrable since the surface is multiply connected. We visualize the discrepancy field $\mathbf{c}$ that characterizes the deviation of the cross field from a curl-free field in the insets, and show that moving singularities along the field direction of $\mathbf{c}$ reduces $\mathbf{c}$, thereby improving integrability. When $\mathbf{c} \equiv \mathbf{0}$, the cross field is both smooth and integrable (c), which naturally induces a global conformal parameterization (d) whose parameter lines are well aligned with the field. Each positive (resp. negative) singularity has a cone angle $\frac{\pi}{4}$ (resp. $\frac{-\pi}{4}$). The area and angle distortion metrics are $E_{AD} = 1.015$ and $E_{SD} = 1.076$, respectively. The closer the distortion metrics to 1, the higher the quality of the parameterization.

surfaces of arbitrary topology. Let Ω be a smooth surface and θ a cross field with the lowest Dirichlet energy defined on Ω. By utilizing the singularities of θ and the boundary (if present) of Ω as boundary conditions, we compute a conformal factor field $\varphi : \Omega \to \mathbb{R}$ by solving a Poisson's equation. Subsequently, we define a vector field $\mathbf{c}$, referred to as the discrepancy field, for all regular points, which quantifies the difference between the gradient of the conformal factor $\nabla\varphi$ and the rotation vector of the cross field θ. In simply connected domains where θ is free of directional constraints, the discrepancy is always a zero vector. In multiply connected domains, $\mathbf{c}$ is globally divergence free and locally curl free. We then prove that a smooth cross field θ is integrable if and only if the discrepancy field vanishes everywhere except at the singularities.

The established necessary and sufficient condition in the continuous setting serves a foundation for a new algorithm for computing integrable cross fields on triangle meshes with non-trivial topology. Our method is fully automatic and supports boundary alignment and sparse hard directional constraints. It also allows the user to balance the number of singularities and the area distortion of the induced conformal parameterization by tuning a parameter r_0, which represents the radius of each singularity modeled as a disk. Through extensive evaluations, we show that the algorithm enables the generation of high-quality global conformal parameterizations that are well aligned with the cross fields. See Fig. 1 for an example of our method.

II. Related Works

For brevity, we restrict our survey to the most relevant works on cross fields, non-orthogonal fields and cone optimization in surface parameterization. For a comprehensive survey of orthogonal and non-orthogonal directional fields, we refer readers to [17].

Cross fields were first introduced by Hertzmann and Zorin as a computational tool for non-photorealistic cross-hatching rendering [3], and later generalized to N-rotational symmetric directional field (N-RoSy) in [1] [2]. Since then, smooth cross and N-RoSy fields have been extensively studied [17]. If singularities are given (i.e., their number, placement and indices are fixed), smooth cross fields can be efficiently created by solving a sparse linear system [8]. The design of cross fields with unknown singularities (number, placement and indices) are often formulated as a non-linear optimization problem with or without integer variables [4], [10], [11], [12], [18], [19].

Cross fields are inherently isometric, meaning they do not encode scale information. Frame fields, representing a more generalized form of cross fields, are characterized by their non-orthogonality and non-unit-lengths. This unique aspect makes frame fields suitable for anisotropic quadrangulation with varying element size [20]. Viewing frame fields as cross fields in a specific Riemannian metric, Jiang et al. [21] first computed a discrete metric on the input surface that is compatible with input constraints and then optimized the cross field in this customized metric to obtain final frame field. Furthermore, 2D singularity-free frame fields have found applications in line drawing vectorization [22].

PolyVectors are sets of vectors that are unordered and represented as the roots of a complex polynomial. A smooth PolyVector field can be computed by solving a sparse linear system without integer variables [23]. By eliminating discrete curls, one can obtain integrable PolyVector fields. These integrable fields are particularly useful for computing global parameterizations that adhere to specific alignment constraints [13]. Sageman-Furnas et al. [15] formulated the global parameterization problem in terms of commuting PolyVector fields, and designed an efficient optimization method to solve it. Based on the modification of holonomic signature loops, Shen et al. [24] developed a method aimed at generating parameterizations that are locally injective and globally holonomic.

Cone singularities play a critical role in controlling the area distortion of surface parameterization. Various heuristics and optimization frameworks have been proposed to automatically determine the singularity configuration [25], [26], [27], [28], [29], [30], [31]. Campen et al. [32] showed that for arbitrary given sets of topologically admissible parametric cones with prescribed curvature, a global seamless parametrization always exists.

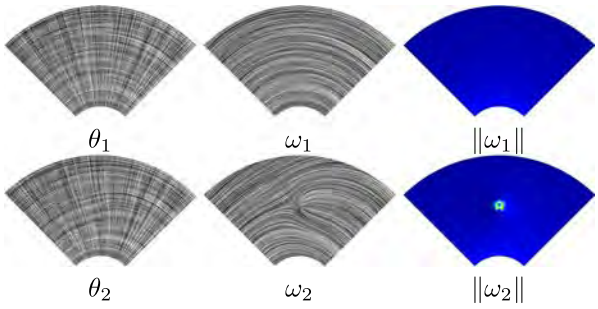

Fig. 2. Cross field and its associated rotation vector field. Top: A smooth cross field θ_1 is generated using boundary constraints only. Its induced rotation field ω_1 has vanishing divergence everywhere. Bottom: In the case of the cross field θ_2, where a directional constraint is added at an interior point, it induces a rotation vector field ω_2 in which that point becomes a source of the rotation field. We visualize the magnitude $\|\omega\|$ using a heat color map, where cold colors indicate small magnitudes and warm colors indicate large magnitudes.

Our paper closely relates to the seminal work of Bunin [14], who developed an elegant algorithm for computing conformal parameterizations of simply connected domains. His method computes the conformal factor φ by solving Poisson's equation with user-provided singularities. The gradient of φ induces an integrable cross field, which yields a conformal parameterization. Manual singularity selection heavily relies on human geometric intuition and trial and error. We extend Bunin's original idea to surfaces of arbitrary topology by addressing the challenge of integrability. Furthermore, our method can automatically determine the singularity configuration and also allows the user to control the number of singularities by tuning a parameter with intuitive meaning.

III. Smooth Cross Fields

A cross field on a surface is defined as a pair of perpendicular tangent directions, with a degree of freedom of 1. Consider a cross field θ defined on a smooth surface Ω. As a cross moves along the field line, it undergoes rotation. To quantify this rotation, we associate a unique vector field ω with θ, where $\omega \cdot \mathrm{d}\mathbf{l}$ represents the rotation angle along the line element $\mathrm{d}\mathbf{l}$, and $\cdot$ denotes the vector dot product. The magnitude of ω indicates the rotation speed. In this paper, we refer to ω as the *rotation vector field* of the cross field θ. It is important to note that the rotation vector ω is undefined at singularities, as its magnitude becomes infinite.

The rotation vector field ω can be seen as analogous to the gradient field of a scalar function, as the cross experiences the highest rotation speed while parallelly transported along ω. However, we cannot express ω as $\nabla\theta$, since θ is not a scalar-valued function and lacks a reference direction unless Ω has zero Gauss curvature everywhere. In Fig. 2, we provide two examples of cross fields and their associated rotation vector fields.

In cross fields, singularities are isolated points where the direction field shows discontinuity, and they are inevitable in all but the simplest shapes. Each singularity, denoted as s_i, is associated with a non-zero index $I(s_i)$. This index, which is a multiple of $\frac{1}{4}$, characterizes the behavior of the cross field in the vicinity of s_i. Fig. 3 illustrates typical types of singularities, with their indices ranging from $-1/2$ to $1/2$. According to the Poincaré-Hopf Theorem, for a closed, orientable surface of genus g, the sum of all the indices of singularities in a cross field equals the Euler characteristic $2-2g$.

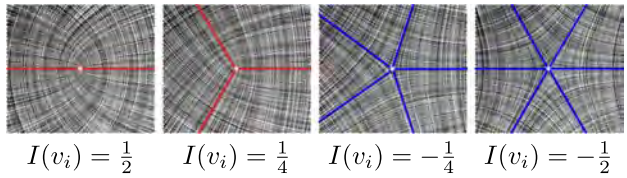

Fig. 3. Illustration of singularities in cross fields. The red and blue curves are the integral curves intersecting the singularity.

By applying the Gauss-Bonnet Theorem, it is easy to see that for an arbitrary simply connected subset $D \subset \Omega$, the rotation vector field ω satisfies the following equation [14]:

$$\oint_{\partial D} \omega \cdot \mathrm{d}\mathbf{l} = -\iint_D K \mathrm{d}\sigma + 2\pi \sum_{s_i \in D} I(s_i), \tag{1}$$

where K is the Gaussian curvature, and $\mathrm{d}\mathbf{l}$ and $\mathrm{d}\sigma$ are the line and area elements, respectively.

Let $\mathcal{S} = \{s_i | s_i \in \Omega\}$ denote the set of singularities of the cross field θ. Equation (1), which represents a constraint on ω in integral form, can also be expressed in differential form as follows:

$$(\nabla \times \omega)(x) \cdot \mathbf{n} = -K(x) + 2\pi \sum_{s_i \in \mathcal{S}} \delta(x - s_i), \tag{2}$$

where x is an interior point of Ω, $\mathbf{n}$ is the surface normal and $\delta(x - s_i)$ denotes the Dirac delta function.

Since the rotation vector ω describes the rotational behavior of the cross field θ between points, excluding singularities, it is natural to use $\|\omega\|^2$ as a measure of the smoothness of θ. The smoothness energy of the cross field θ is then defined as:

$$E_{\text{smooth}} = \iint_\Omega \|\omega\|^2 \, \mathrm{d}A. \tag{3}$$

By applying the variational method to (3), it becomes apparent that if the cross field θ has a locally minimal smoothness energy, the corresponding rotation vector field ω must be divergence-free, satisfying the condition:

$$\nabla \cdot \omega = 0. \tag{4}$$

We define the smoothness of a cross field θ by the condition that its associated rotation vector field ω satisfies (4). All subsequent discussions regarding cross field in this paper assume their smoothness, as this is a prerequisite for the application of Bunin's theory.

IV. Simply-Connected Domains

As our work builds upon the theoretical framework established by Bunin [14], we provide a brief overview of his key findings. Throughout this section, we refer to Ω as a simply connected domain.

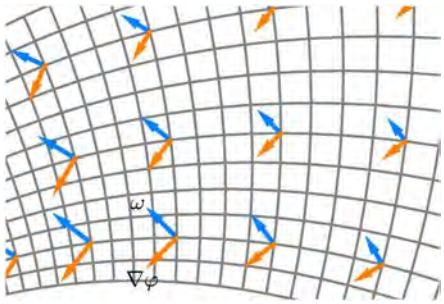

Fig. 4. Gradients of a boundary-aligned conformal parameterization.

A. Boundary-Aligned Conformal Parameterization

Let $\mathbf{r}(u,v):\mathbb{R}^2\to\Omega$ be a conformal parametrization of Ω, where the parameter lines are aligned with the domain boundary $\partial\Omega$. The tangent vectors $\mathbf{r}_u$ and $\mathbf{r}_v$ are orthogonal:

$$\mathbf{r}_u \perp \mathbf{r}_v$$

and have equal lengths:

$$\|\mathbf{r}_u\| = \|\mathbf{r}_v\|.$$

Thus, the normalized tangent vectors $(\alpha,\beta) = (\mathbf{r}_u/\|\mathbf{r}_u\|, \mathbf{r}_v/\|\mathbf{r}_v\|)$ form a cross field[1] on Ω.

Since the parameterization $\mathbf{r}$ is aligned with the surface boundary $\partial\Omega$, the cross field should rotate by an angle equal to the geodesic curvature of the boundary when traversing along $\partial\Omega$. Consequently, the associated rotation vector ω satisfies the equation

$$\omega\cdot\mathbf{t} = \kappa_g$$

for all boundary points, where $\mathbf{t}$ represents the unit tangent vector along $\partial\Omega$ and κ_g denotes the geodesic curvature.

The conformal factor $e^{-\varphi}$, defined as

$$e^{-\varphi} = \|\mathbf{r}_u\|,$$

characterizes the local cell size. Intuitively, the gradient $\nabla\varphi$ (illustrated in orange in Fig. 4) represents the direction in which the rate of change in cell size is highest.

Bunin proved that for simply connected domains, the gradient of the conformal factor φ at interior points is perpendicular to the rotation vector, as expressed by the equation:

$$\nabla\varphi = \mathbf{n}\times\omega, \tag{5}$$

where $\mathbf{n}$ the outward normal of Ω. At any boundary point, the condition

$$\nabla\varphi\cdot\mathbf{n}_b = \kappa_g$$

holds, where $\mathbf{n}_b$ is the normal of the boundary $\partial\Omega$.

Substituting (5) into (1), we obtain the following integral equation:

$$\oint_{\partial\Omega}\nabla\varphi\cdot\mathbf{n}_b\mathrm{d}l = -\iint_{\Omega}K\mathrm{d}\sigma + 2\pi\sum_{s_i\in\Omega}I(s_i), \tag{6}$$

[1]For notation purposes, we use a 2-tuple of orthogonal vectors to denote a cross field, aligning them with the gradients of the u and v parameters.

Since Ω is simply connected, applying the Gauss-Bonnet Theorem results in

$$\sum_{s_i\in\Omega}I(s_i) = \frac{1}{2\pi}\left(\iint_{\Omega}K\mathrm{d}\sigma + \oint_{\partial\Omega}\kappa_g\mathrm{d}l\right) = 1. \tag{7}$$

Equation (7) is a necessary condition for the singularities of a conformal parameterization on a simply connected domain. Bunin showed that this condition is also sufficient [14]. Therefore, provided that a set of singularities satisfies (7), a unique conformal parametrization exists, with parameter lines that are aligned with the domain boundary.

Since $\|\nabla\varphi\| = \|\omega\|$, the smoothness energy of the cross field θ is equivalent to the Dirichlet energy of the conformal factor

$$E_{\text{smooth}}(\omega) = E_{\text{Dirichlet}}(\varphi),$$

highlighting the profound relationship between smooth cross fields and boundary-aligned conformal parameterizations.

Note that (5) immediately implies the following:

$$\begin{aligned}\nabla\cdot\omega &= \nabla\cdot(\nabla\varphi\times\mathbf{n})\\ &= (\nabla\times\nabla\varphi)\cdot\mathbf{n} - \nabla\varphi\cdot(\nabla\times\mathbf{n})\\ &= 0,\end{aligned}$$

which confirms that the rotation vector field ω is divergence-free as specified in (4). Bunin also proved that for simply connected domains, the condition $\nabla\cdot\omega = 0$ is sufficient for θ to be smooth. Therefore, computing a boundary-aligned conformal parameterization in simply connected domains is equivalent to constructing a smooth cross field. In other words, for a cross field with a divergence-free ω, there always exists a conformal factor to make it integrable.

B. Bunin's Algorithm

Given a set of singularities that satisfy (7) within a simply-connected domain, Bunin's algorithm initiates by solving the differential form of (6), which is Poisson's equation

$$\nabla\cdot\nabla\varphi(x) = 2\pi\sum_{s_i\in\mathcal{S}}\delta(x-s_i) - K(x), \tag{8}$$

for an interior point $x\notin\partial\Omega$. The boundary condition applied to points $x\in\partial\Omega$ is the Neumann condition:

$$\nabla\varphi(x)\cdot\mathbf{n}_b = \kappa_g(x). \tag{9}$$

After determining the conformal factor $e^{-\varphi}$, Bunin constructed a cross field θ using the gradient $\nabla\varphi$. Since the cross field θ is integrable, the conformal parameterization can be achieved by integrating the field lines of θ.

V. Multiply-Connected Domains

In simply-connected domains, Bunin showed that a conformal factor φ satisfying (8) and (9) can ensure the existence of a cross field with a rotation vector ω perpendicular to $\nabla\varphi$. Unfortunately, this property does not extend to multiply-connected domains. The primary distinction between simply- and multiply-connected domains is that not every simple loop in a multiply-connected domain encloses a region.

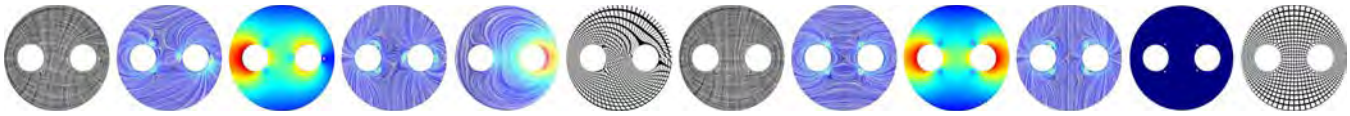

Fig. 5. Smoothness does not automatically imply integrability in multiply connected domains. (a) Consider a cross field $\theta_1 = (\alpha, \beta)$ with locally minimal smoothness energy defined on a two-holed disc. There are four singularities of indices $\frac{-1}{4}$. (b) The associated rotation vector field ω_1 is divergence-free. (c) Using the singularities of θ_1, we compute the conformal factor $e^{-\varphi_1}$ by solving Poisson's equation (8). (d) The gradient $\nabla\varphi_1$ is not perpendicular to the rotation vector ω_1. (e) Consequently, the discrepancy field $\mathbf{c}_1 = \nabla\varphi_1 - \mathbf{n} \times \omega_1$ does not vanish, indicating that the cross field θ_1 is not integrable. (f) As a result, the induced parameterization (u_1, v_1), which is the minimizer of $\|\nabla u_1 - \alpha\|^2 + \|\nabla v_1 - \beta\|^2$, is neither conformal nor aligned with θ_1. (g-k) Optimizing the locations of singularities can significantly reduce the discrepancy field, leading to an integrable cross field θ_2. (l) shows the induced conformal parameterization (u_2, v_2) that is well aligned with the cross field θ_2.

In a multiply-connected domain, Ω, consider a scalar function $\varphi : \Omega \to \mathbb{R}$ satisfying (8) and let θ be an integrable cross field sharing the same singularities of φ. Consider a simple loop $C \subset \Omega$ that does not pass through any singularity. Parallel transport of a cross along C returns to the starting point with the cross overlapping its initial position, implying that the angle change in parallel transport along C is a multiple of $\frac{\pi}{2}$ radians:

$$\oint_C (\omega \cdot \mathbf{t} - \kappa_g)\, \mathrm{d}l = \frac{k\pi}{2},$$

for some integer $k \in \mathbb{Z}$, where $\mathbf{t}$ is the unit tangent vector, and κ_g is the geodesic curvature of C. Assuming the rotation vector ω of the cross field θ is perpendicular to the gradient $\nabla\varphi$, the scalar function φ must then satisfy the following condition:

$$\oint_C (-\nabla\varphi \cdot \mathbf{n}_b - \kappa_g)\, \mathrm{d}l = \frac{k\pi}{2}, k \in \mathbb{Z} \tag{10}$$

where $\mathbf{n}_b$ is the normal vector along the loop C. Equation (10) represents an *additional* condition that φ must meet to ensure the existence of an integrable cross field θ where ω is perpendicular to $\nabla\varphi$.

Applying Green's theorem and the Gauss-Bonnet theorem, it can be demonstrated that (10) holds automatically if C is the boundary of a simply connected domain and φ satisfies (8). Consequently, this condition is redundant for simply connected domains, where the inherent topological and geometric properties ensure the required integrability without the need for additional constraints.

However, (10) does not automatically hold if C does not border a region. Fig. 5 provides an example where φ, defined on a two-holed annulus, satisfies (8) but its gradient $\nabla\varphi$ does not satisfy (10). This illustrates that Bunin's algorithm is specially applicable only to simply-connected domains, as it relies on certain topological characteristics that are absent in more complex geometries.

Let S be a smooth surface. To obtain a conformal parameterization that is well aligned with a given cross field $V = (\alpha, \beta)$, V must be integrable. Local integrability of the direction field is a necessary condition for seamless parametrization. Specifically, a cross field on a smooth surface S is integrable if there exist scalar functions $u : S \to \mathbb{R}$, $v : S \to \mathbb{R}$, $\lambda : S \to \mathbb{R}_+$ and $\mu : S \to \mathbb{R}_+$ such that $\nabla u = \lambda\alpha$ and $\nabla v = \mu\beta$, where ∇ is the gradient operator. In other words, a cross field is integrable if it satisfies the curl-free condition. According to the Frobunius theorem, the local integrability condition is equivalent to

$$\mu\beta \cdot \nabla\lambda\alpha = \lambda\alpha \cdot \nabla\mu\beta.$$

If the cross field V contains singularities or if the surface has a non-disk topology, it is necessary to cut S open into a single patch with disk topology, placing all singularities on its boundaries. Although the function values u (respectively, v) may be discontinuous across the seams, seamless parameterization can still be achieved as long as the gradients ∇u (respectively, ∇v) align across these seams.

We define the *discrepancy* field to measure the difference between the gradient of the conformal factor and the cross field's rotation vector,

$$\mathbf{c} \triangleq \nabla\varphi - \mathbf{n} \times \omega. \tag{11}$$

We prove a smooth cross field is integrable if and only if the discrepancy vanishes everywhere except at the singularities.

Theorem 1: Let S be a smooth surface of arbitrary topology, and let $\theta = (\alpha, \beta)$ be a smooth and boundary-aligned cross field defined on S. The cross field θ is integrable if and only if its discrepancy vector $\mathbf{c} = \mathbf{0}$ vanishes for all regular points.

VI. Continuous Setting

Building on our theoretical insights, we develop a new approach for automatically computing a smooth and integrable cross field. This method is designed to

- aligns with the surface's boundaries and adhere to the user-specified directional constraints;
- incorporate a set of singularities to ensure the resulting conformal parameterization exhibits low area distortion; and
- function effectively across surfaces with complex topology.

Throughout our algorithm, we model singularities as moving geodesic disks and iteratively adjust their number, indices, and locations. This feature distinguishes our method from traditional optimization-based methods.

Initiated with a random cross field, which typically contains a large amount of singularities due to initial non-smoothness, our method begins by constructing a smooth cross field θ through the minimization of the Dirichlet energy (3). As the process unfolds, singularities of opposite signs attract each other and annihilate upon contact.

Although θ achieves locally minimal Dirichlet energy, it may not be integrable in multiply-connected domains. To eliminate

curls in θ, we fix the indices and the number of singularities, then proceed to optimize their locations.

We document the key technical aspects of our algorithm in this section and present the corresponding pseudocode. For implementation details, we refer readers to the supplementary material.

A. Computing Smooth Cross Fields

1) Singularity Movement: Starting with a randomly initialized cross field $\theta^{(0)}$, we first compute the conformal factor φ by solving Poisson's (8) with the singularities of θ. The gradient $\nabla\varphi$ and its $i\frac{\pi}{2}$ rotations, $i = 1, 2, 3$, generate a new cross field $\theta^{(1)}$, which is noticeably smoother than $\theta^{(0)}$.

Let $\omega^{(1)}$ be the rotation vector field of $\theta^{(1)}$. Given that $\|\omega^{(1)}\| = \|\nabla\varphi\|$, the smoothness of cross field $\theta^{(1)}$ corresponds to the Dirichlet energy of φ. As noted by Knöppel et al. [11], $\|\nabla\varphi\| \to \infty$ approaches infinity at singularities. Therefore, to achieve finite energy, it is necessary to exclude the singularities. We model each singularity s_i as a geodesic disk $D_{r_0}(s_i)$ and define the smoothness energy for $\theta^{(1)}$ as:

$$E_{\text{smooth}}(\theta^{(1)}, r_0) = \iint_{\Omega \setminus \bigcup_{s_i \in \mathcal{S}} D_{r_0}(s_i)} \|\nabla\varphi\|^2 \mathrm{d}A. \tag{12}$$

The disk radius r_0, which is a user-specified parameter, plays a critical role in controlling the number of singularities and the area distortion of the resulting conformal parameterization.

Notice that $\nabla\varphi$ is implicitly controlled by two main factors: 1) the Gaussian curvature K of the domain Ω and 2) the singularities within the field. Since altering K is not allowed, a possible way for reducing the Dirichlet energy of $\theta^{(1)}$ involves modifying the singularities.

If singularities were merely isolated points, moving a singularity would be straightforward, since the direction of the movement would be clearly defined. However, as mentioned earlier, we model singularities as geodesic disks to ensure finite Dirichlet energies. Therefore, it becomes necessary to consider the individual "force" acting on every point within the geodesic disk and then compute a combined "force" to effectively move the entire disk. Specifically, we calculate the area integral as follows:

$$\mathbf{F}(s_i) = \iint_{D_{r_0}(s_i)} (\nabla \cdot \nabla\varphi)\nabla\varphi \mathrm{d}A.$$

In the supplementary material, we show that the above area integral is equivalent to a boundary loop integral:

$$\mathbf{F}(s_i) = \oint_{\partial D_{r_0}(s_i)} \mathbf{T} \cdot \mathbf{n} \mathrm{d}l, \tag{13}$$

where $\mathbf{T}$ is the Maxwell tensor:

$$\mathbf{T} = \nabla\varphi \otimes \nabla\varphi - \frac{1}{2}\|\nabla\varphi\|^2 \mathbf{I}. \tag{14}$$

We then move the singularity s_i in the direction of the computed force $\mathbf{F}(s_i)$. When two singularities of opposite indices encounter one another, they annihilate, leading to a significant reduction in the smoothness energy. Additionally, a singularity with an index $\pm\frac{1}{2}$ can split into two singularities, each with an index $\pm\frac{1}{4}$.

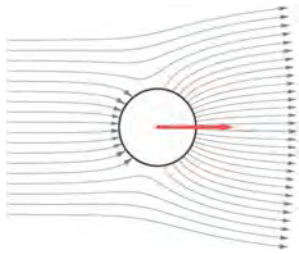

Fig. 6. Illustration of the forces acting on a singularity. Each singularity is represented as a 2D disk $D_{r_0}(s_i)$, with the surrounding gradient field $\nabla\varphi$ depicted. The force acting on the singularity is computed via a boundary integral, which drives the singularity to move.

Once all singularities cease moving, the smoothness energy reaches a local minimum, and the resulting cross field θ achieves a state of smoothness.

Remark 1: To comprehend why moving singularities reduces the smoothness energy, consider the vicinity of $D_{r_0}(s_i)$ for a singularity s_i as shown in Fig. 6. In the absence of s_i, the field $\nabla\varphi_0$ might be approximated as evenly distributed around $D_{r_0}(s_i)$. The presence of s_i introduces a radial component $\nabla\varphi_1$, augmenting the original field. This configuration means that on the side where $\nabla\varphi_0$ and $\nabla\varphi_1$ align, they collaboratively strengthen $\nabla\varphi$, thereby enhancing the field intensity. Conversely, on the side where $\nabla\varphi_0$ and $\nabla\varphi_1$ oppose each other, they act to weaken $\nabla\varphi$, reducing the field's strength. By moving the singularity in the direction of the force, we decrease the area where $\|\nabla\varphi\|$ is large and increase the area where $\|\nabla\varphi\|$ is small, leading to a reduction in the Dirichlet energy. Another perspective to explain the reduction in smoothness energy involves viewing singularities as charged particles and the gradient field $\nabla\varphi$ as an electrostatic field. Thus, moving these charged particles under electrostatic forces effectively reduces the total potential energy, which is equivalent to the smoothness energy.

2) Global Singularity Pairing: We observe that on surfaces with simple geometry, where Gaussian curvatures maintain consistent signs, electric-like forces can effectively guide singularities to globally optimal positions, as shown in Fig. 13. However, on general surfaces characterized by a mixture of positive and negative Gaussian curvatures, singularities tend to become trapped in locally optimal positions. This is due to the electrostatic-like forces driving them only locally, lacking the capacity to merge two singularities that are distant from each other (refer to Fig. 7).

To overcome this challenge, we propose a simple yet effective heuristic that operates on a *large* scale to merge singularities. Specifically, we identify two vertices, $v_{\max}$ and $v_{\min}$, which posses the largest and smallest conformal factors, respectively, and label them as the *peak* and the *valley* (see Fig. 8). We then compute the shortest path $\gamma(v_{\max}, v_{\min})$ between them and proceed to neutralize the value difference by moving $v_{\max}$ and $v_{\min}$ towards each other along γ.

Since the peak $v_{\max}$ and the valley $v_{\min}$ are not necessarily singularities, we consider four cases:

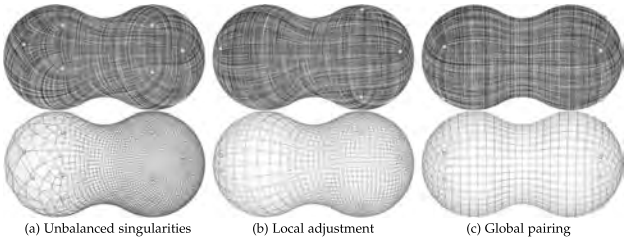

Fig. 7. Local adjustment vs global pairing. (a) On a symmetric peanut-shaped surface, we initially create a smooth cross field with unbalanced singularities: 4 positive and 2 negative singularities on the left side, and 6 positive on the right. (b) Using only local adjustments, two negative singularities merge with two nearby positive ones, resulting in 4 singularities on the left. However, the additional singularities on the right remain isolated, maintaining an imbalance in the cross field. (c) With the global pairing strategy, singularities are driven on a much large scale, achieving a balanced distribution with 4 singularities on each side. As a result, the area distortion of the induced conformal parameterization is also reduced significantly. The top and bottom rows illustrate the cross fields and their corresponding parameterizations, respectively.

Fig. 8. This illustration compares two sets of singularities with identical indices but varying radii. The singularities on the left feature larger radii compared to those on the right. The set with smaller radii generates a more intense vector field, $\nabla\varphi$, characterized by steeper peaks and deeper valleys in the value of φ. We depict φ using a color-coded height function to visually represent these variations.

- *Case 1:* Both $v_{\max}$ and $v_{\min}$ are regular vertices. A pair of singularities with opposite signs are created, i.e., a negative singularity at $v_{\max}$ and a positive singularity at $v_{\min}$, increasing the total number of singularities by 2.
- *Case 2:* $v_{\max}$ is a positive singularity and $v_{\min}$ is regular. The singularity is moved from $v_{\max}$ to $v_{\min}$, transforming $v_{\max}$ into a regular vertex and $v_{\min}$ into a positive singularity.
- *Case 3:* $v_{\max}$ is regular and $v_{\min}$ is a negative singularity. The singularity is moved from $v_{\min}$ to $v_{\max}$, transforming $v_{\min}$ into a regular vertex and $v_{\max}$ into a negative singularity.
- *Case 4:* Both $v_{\max}$ and $v_{\min}$ are singularities. The two singularities annihilate, reducing the number of singularities by 2.

The radius of the geodesic disk, r_0, significantly impacts the behavior of singularities. When comparing two disks centered at the same point but with different radii, the smaller disk exhibits a higher Dirichlet energy due to a larger integration domain. A smaller radius r_0 not only increases the Dirichlet energy but also accentuates the peak and valley of the conformal factor φ. This intensification raises the likelihood that both $v_{\max}$ and $v_{\min}$ will manifest as singularities (as seen in case 4), thereby reducing the overall number of singularities. Conversely, a larger radius r_0 leads to a lower Dirichlet energy, which results in more evenly distributed peaks and valleys of φ. This distribution increases the probability of $v_{\max}$ and $v_{\min}$ being regular (as in case 1), and Since two new singularities are created in this scenario, it ultimately increases the total number of singularities. In our algorithm, users can adjust r_0 to control the number of singularities effectively.

Remark 2: Our global pairing strategy bears similarities to Ben-Chen et al.'s method [25], which iteratively adds singularities at locations exhibiting the largest differences in the conformal factor. Their algorithm terminates once the conformal factor difference falls below a user-specified threshold. Similarly, our global pairing strategy targets the vertex pair with the greatest conformal factor difference. However, our approach allows these vertices to move towards each other along a defined path. Upon meeting, they significantly alter the conformal factor field. If this new field configuration results in lower energy, it is retained. Subsequent local adjustments of singularities are then performed to further decrease the Dirichlet energy. Our method concludes when additional global pairing fails to produce a cross field with reduced energy.

B. Eliminating Curls

Minimizing the Dirichlet energy produces a smooth cross field, which in general contains curls if the domain is multiply connected. As discussed above, the key challenge is that in a multiply-connected domain, the rotation vector ω of a smooth cross field θ may not be perpendicular to the gradient of φ, even though φ satisfies (8) and shares the same set of singularities as θ (see Fig. 5(a)–(d)).

To characterize the misalignment between ω and $\nabla\varphi$, we define a vector field $\mathbf{c}$ as follows:

$$\mathbf{c} = \nabla\varphi - \mathbf{n} \times \omega, \tag{15}$$

where $\mathbf{n}$ is the unit outward normal of Ω. Clearly, if $\mathbf{c} \equiv 0$, the cross field θ is integrable. In the following, we first examine the properties of $\mathbf{c}$, and then present our method to eliminate curls in θ.

1) Properties: Given that ω and φ share the same set of singularities, subtracting (2) from (8) results in $(\nabla \times \omega) \cdot \mathbf{n} = \nabla \cdot \nabla\varphi$. To analyze the divergence of $\mathbf{c}$, we calculate:

$$\begin{aligned} \nabla \cdot \mathbf{c} &= \nabla \cdot (\nabla\varphi - \mathbf{n} \times \omega) \\ &= \nabla \cdot \nabla\varphi - (\nabla \times \mathbf{n}) \cdot \omega - \mathbf{n} \cdot (\nabla \times \omega) \\ &= 0, \end{aligned} \tag{16}$$

confirming that $\mathbf{c}$ is divergence-free.

Additionally, since θ is a local minimizer of E_{smooth}, we have $\nabla \cdot \omega = 0$. Computing curl of $\mathbf{c}$ gives:

$$\begin{aligned} \nabla \times \mathbf{c} &= \nabla \times (\nabla\varphi - \mathbf{n} \times \omega), \\ &= \nabla \times \nabla\varphi - \nabla \times (\mathbf{n} \times \omega) \\ &= \mathbf{0}. \end{aligned} \tag{17}$$

Therefore, the vector field $\mathbf{c}$ is also *locally* curl-free. This implies that there are no sources and sinks in $\mathbf{c}$, and each integral curve of $\mathbf{c}$ forms a closed loop.

We show that moving the singularities along the field lines of $\mathbf{c}$ reduces the energy $\iint \|\mathbf{c}\|^2 \mathrm{d}A$. Therefore, a straightforward

approach might involve computing forces for all singularities and moving them incrementally along the field lines with small time steps. This process is repeated until all singularities cease movement. While conceptually simple, this method is time-consuming because the forces act locally and only update the singularities in their immediate vicinity. To enhance efficiency, we propose a two-step approach: in the first step (discrete adjustment), we rotate the cross field θ while maintaining the fixed locations of singularities. This action results in a significant alteration of $\mathbf{c}$. Subsequently, in the second step (continuous adjustment), we move the singularities along the field lines. This modifies $\|\mathbf{c}\|$ in a continuous manner.

2) Discrete Adjustment: Consider C, a non-contractible loop that passes no singularity and exhibits a consistent sign for $\int \mathbf{c} \cdot \mathrm{d}\mathbf{l}$. Denote by C^+ as the side where $\mathbf{c} \cdot \mathrm{d}\mathbf{l} > 0$ and C^- as the opposite side. We compute the rotation angle ψ by solving Laplace's equation

$$\triangle \psi = 0 \tag{18}$$

with the Dirichlet boundary condition

$$\psi|_{C^+} - \psi|_{C^-} = \frac{\pi}{2}. \tag{19}$$

We then rotate the cross field θ by an angle ψ. Since ψ is a solution of Laplace's equation, the rotated cross field remains smooth. Additionally, due to the boundary condition (19) and the rotational symmetry of the cross field, it is continuous across C.

To understand how this rotation impacts $\mathbf{c}$, let us compute the loop integral J that quantifies the strength of $\mathbf{c}$:

$$\begin{aligned} J &= \oint_{C^+} \mathbf{c} \cdot \mathrm{d}\mathbf{l} = \oint_{C^+} \nabla\varphi \cdot \mathrm{d}\mathbf{l} - \oint_{C^+} \omega \cdot \mathbf{n}_b \mathrm{d}l \\ &= -\oint_{C^+} \omega \cdot \mathbf{n}_b \mathrm{d}l, \end{aligned}$$

where $\mathbf{n}_b$ is the outward normal of C. The last equality follows because φ is a single-valued function and its gradient is curl free, implying no net circulation around C. J is positive due to the chosen orientation of C^+ and can thus be interpreted as the inward flux of the vector field ω.

When θ is rotated by ψ, the vector field ω is modified by $\nabla\psi$. Consequently, the value of J is adjusted to:

$$J = -\oint_{C^+} (\omega + \nabla\psi) \cdot \mathbf{n}_b \mathrm{d}l.$$

This adjustment results in a sharp change in J due to the rotation.

3) Continuous Adjustment: In the continuous adjustment phase, we move singularities along the field lines of $\mathbf{c}$. To understand why moving singularities reduces $\mathbf{c}$, consider a non-contractible loop L that does not intersect any singularities. We calculate the flux of $\mathbf{c}$ across L as follows:

$$I = \oint_L \mathbf{c} \cdot \mathbf{n}_b \mathrm{d}l = \oint_L \nabla\varphi \cdot \mathbf{n}_b \mathrm{d}l - \oint_L \omega \cdot \mathbf{t} \mathrm{d}l,$$

where $\mathbf{n}_b$ is the normal vector to L and $\mathbf{t}$ is the tangent vector to L. This flux I measures the net number of field lines passing through L, effectively indicating the strength of the field $\mathbf{c}$. The term $\oint_L \omega \cdot \mathbf{t} \mathrm{d}l$ is a constant multiple of $\frac{\pi}{2}$ radians, thus, the primary contribution to I comes from the first integral.

Now, let us consider the movement of a singularity s near L. Define L_{in} as the side where $\mathbf{c}$ enters the loop and L_{out} as the side where $\mathbf{c}$ exits. There are four scenarios to consider based on the location of s and the sign of its index $I(s)$:

- If $I(s) < 0$ and s is on the L_{in} side, moving s along $-\mathbf{c}$ leads it away from L. This reduces the contribution of $\nabla\varphi$ to I, thereby decreasing I. See Fig. 12(a).
- If $I(s) > 0$ and s is on the L_{in} side, moving s along $\mathbf{c}$ brings it closer to L. Since $\nabla\varphi$ and $\mathbf{c}$ are of opposite directions for points on L, the contribution of $\nabla\varphi$ to I decreases, reducing I. See Fig. 12(b).
- If $I(s) < 0$ and s is on the L_{out} side, moving s along $-\mathbf{c}$ brings it closer to L. As $\nabla\varphi$ and $\mathbf{c}$ are of opposite directions for points on L, this decreases I. See Fig. 12(c).
- If $I(s) > 0$ and s is on the L_{out} side, moving s along $\mathbf{c}$ drives it away from L, decreasing the contribution of $\nabla\varphi$ to I and thus reducing I. See Fig. 12(d).

To sum up, we effectively reduce the flux I by moving positive singularities in the direction of $\mathbf{c}$ and negative singularities in the opposite direction, $-\mathbf{c}$, as illustrated in Fig. 11. The divergence-free property of $\mathbf{c}$ ensures that any two cycles belonging to the same homology class will exhibit equal flux. Thus, reducing the flux for a specific cycle L inherently reduces the flux for all cycles homologous to L.

VII. Discrete Algorithm

Our algorithm consists of three steps, which are detailed as follows.

Step 1. Initializing θ: For boundary faces and faces with user-specified directional constraints, we establish fixed crosses aligned with the given direction. For all other faces, we generate random crosses to initiate the field configuration.

Step 2. Computing Smooth Cross Field: We begin by taking the singularities of the initial random cross field as input. We then solve Poisson's (8) to compute the initial conformal factor φ. Next, we identify the vertices $v_{\max}$ and $v_{\min}$, which have the highest and lowest values of φ, respectively. We merge these vertices along a simple path and subsequently update the field $\nabla\varphi$. Following this, we move the singularities along the field lines determined by the updated $\nabla\varphi$. This process continues until the singularities cease moving, indicating that φ has reached a locally minimal Dirichlet energy. If the newly computed energy is lower than the previously recorded energy, the merging of $v_{\max}$ and $v_{\min}$ is deemed successful. The algorithm then proceeds to merge another pair of vertices that exhibit the largest difference in φ values and repeats the merging process. This step is terminated after $k_{\max}$ consecutive failed merging attempts, where we set $k_{\max} = 3$ in our implementation. See Algorithm 1 for the pseudocode.

Step 3. Eliminating Curls: The smooth cross field θ produced in Step 2 may not be integrable if the surface has a non-disk topology. The discrepancy field $\mathbf{c} = \nabla\varphi - \mathbf{n} \times \omega$ quantifies the curls within θ. The objective of this step is to reduce the

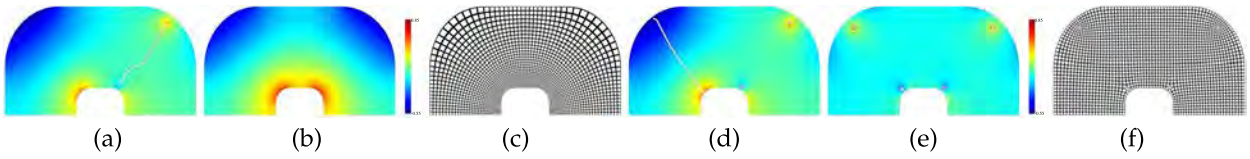

Fig. 9. The disk radius r_0 plays a critical role in computing smooth cross fields. This toy model features one positive and one negative singularity, represented as orange and blue spheres, respectively. Using the same conformal factor φ, we experiment with a small radius in (a) and a large radius in (d). Let A be the surface area. With a small radius $r_0 = \sqrt{A}10^{-3.5}$, the smoothness energy is $E^{(a)} = 3.816$. Since both $v_{\max}$ and $v_{\min}$ are singular, applying the global pairing strategy results in annihilation (case 4), producing a singularity-free cross field (b) with energy $E^{(b)} = 3.009 < E^{(a)}$. The corresponding parameterization is shown in (c). With a large radius $r_0 = \sqrt{A}10^{-2.0}$, the smoothness energy is $E^{(d)} = 2.460$. Since both $v_{\max}$ and $v_{\min}$ are regular, pairing them creates a pair of singularities with opposite signs (case 1). This results in a cross field with four singularities show in (e) and a Dirichlet energy of $E^{(e)} = 2.019 < E^{(b)}$. Consequently, the induced parameterization in (f) exhibits lower area distortion than (c).

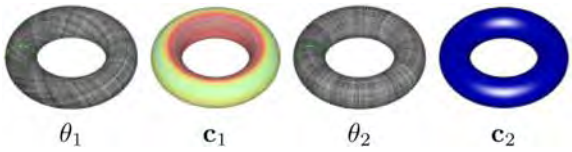

Fig. 10. Discrete adjustment of the cross field. The initial cross field, θ_0, is smooth but non-integrable due to $\mathbf{c}_1 \neq \mathbf{0}$. We compute the rotation angle ψ by solving Laplace's equation (18) with the Dirichlet boundary condition (19) along C (green curve). The rotated cross field, θ_2, maintains smoothness and continuity along C. Moreover, its discrepancy field $\mathbf{c}_2$ vanishes, rendering θ_2 integrable.

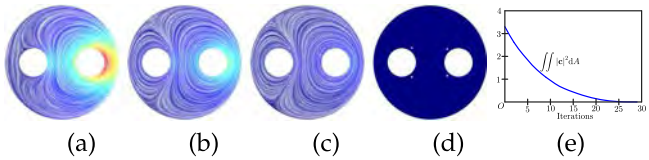

Fig. 11. Curl elimination. (a)–(d) show the discrepancy field $\mathbf{c}$ at the initial state and after the 10-th, 20-th and 29-th iterations, respectively. (e) displays the plot of the curl energy $\iint \|c\|^2$ across these iterations. These visuals demonstrate that adjusting the positions of the singularities progressively reduces the curl energy, thereby enhancing the integrability of the cross field.

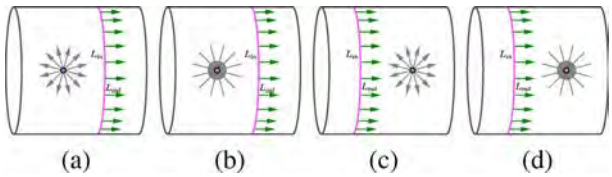

Fig. 12. Continuous adjustment. Moving singularities along the field lines effectively reduces $\mathbf{c}$. A positive (orange) singularity, representing a local maximum of φ, occurs where $\nabla \cdot \nabla\varphi < 0$, causing the gradients $\nabla\varphi$ to converge towards the singularity. Conversely, a negative (blue) singularity, indicating a local minimum of of φ, occurs where $\nabla \cdot \nabla\varphi > 0$, leading the gradients $\nabla\varphi$ to diverge from the point.

magnitude of $\mathbf{c}$ to zero where possible, thereby enhancing the integrability of the field (see Fig. 15). This is accomplished by first computing a global rotation of θ to align it more closely with the gradient $\nabla\varphi$, followed by adjusting the locations of the singularities to further diminish the magnitude of $\mathbf{c}$.

3.1 Discrete adjustment: We employ a trial-and-error approach for discrete adjustments. We identify a point p with the highest $\|\mathbf{c}\|$ and a non-contractible loop C passing through p with a consistent sign of $\int \mathbf{c} \cdot \mathrm{d}\mathbf{l}$. Using C as the boundary condition, we solve Laplace's equation $\triangle\psi = 0$ (18). After rotating θ and ω by angle ψ, we evaluate the curl energy:

$$E_{\mathbf{c}} = \iint_M \|\mathbf{c}\|^2 \mathrm{d}\sigma,$$

which can be viewed as a potential energy of $\mathbf{c}$. If this energy is reduced compared to the previous value, the adjustment is retained. This coarse adjustment continues until no further energy reductions are achieved.

3.2 Continuous adjustment: We refine the singularities' positions iteratively to further minimize $\|\mathbf{c}\|$. Each singularity s is assigned an electrostatic force, $2\pi I(s)\mathbf{c}(s)$. Each iteration targets a singularity s_i exerting the greatest force and moves it along its field line. Movement continues only if the force during each iteration exceeds the previously recorded force for that mesh edge, avoiding endless loops. This step terminates when no further movement of singularities is possible. If the resulting energy $E_{\mathbf{c}}$ is low, the cross field is deemed both smooth and integrable. If not, the user may need to revise or remove some directional constraints to achieve compatibility. Further details and computational steps are outlined in Algorithm 2.

Remark 3: Our algorithm is designed with simplicity in mind, featuring only one model-dependent parameter: the disk radius r_0. This parameter directly controls the number of singularities, which consequently affects the area distortion of the conformal parameterization. Once this parameter is set, the algorithm functions fully automatically, eliminating the need for any further user intervention.

Remark 4: It is worth noting that since $\|\mathbf{c}\|$ is finite at singularities, we do not need to exclude singularities when calculating the curl energy $E_{\mathbf{c}}$. Furthermore, $E_{\mathbf{c}}$ is unitless as the unit of $\|\mathbf{c}\|$ corresponds to the reciprocal of edge length, which simplifies some of the computational considerations.

Remark 5: Although the discrete setting aligns closely with the continuous setting in principle, there are two practical differences that necessitate careful attention in our algorithm design. First, in the continuous setting, singularities are treated as moving geodesic disks with a radius r_0, which requires computing geodesic distances-a computationally expensive task. To streamline our implementation in the discrete setting, we model singularities as vertices along with their 1-ring neighboring triangles. This simplifies the computation of the smoothness energy E_{smooth}, where we initially compute the area integral excluding the 1-ring triangles incident to the singularities and subsequently apply a compensation term for each singularity to

Algorithm 1: Computing Smooth Cross Fields.

Data: A triangular mesh $M = (V, E, F)$, the disk radius r_0, and (optional) sparse hard directional constraints defined on triangular faces
Result: A smooth cross field θ
/* Initialization */
for each face $f \in F$ **do**
  if f is on the boundary **then**
    generate a fixed cross using the boundary direction on f;
  else if f has a directional constraint **then**
    generate a fixed cross using the constraint on f;
  else
    generate a random cross on f;
end
Factor the Laplacian matrix using Cholesky decomposition;
/* Smoothing θ via iterative singularity adjustment */
$k = 0$; $E_{\min} = \infty$; $\theta^* = \theta$;
while $k < k_{\max}$ **do**
  Compute conformal factor φ using the singularities of θ;
  Find $v_{\max}$ and $v_{\min}$ with the largest and smallest φ;
  Find a shortest path γ from $v_{\max}$ to $v_{\min}$;
  for every edge $e_{ij} \in \gamma$ **do**
    /* Assume v_i (resp. v_j) is close to $v_{\max}$ (resp. $v_{\min}$) */
    Move singularity from v_i to v_j;
  end
  Re-compute φ using the singularities of θ;
  for each edge $e_{ij} \in E$ **do**
    /* F_{ij} records the maximal force on edge e_{ij} so far */ $F_{ij} = 0$;
  end
  do
    done = true
    for each singularity s_i **do**
      Compute Maxwell tensor $\mathbf{T} = \nabla\varphi \otimes \nabla\varphi - \frac{1}{2}\|\nabla\varphi\|^2\mathbf{I}$;
      Compute force $\mathbf{F}(s_i) = \oint_{\partial D_{r_0}(s_i)} \mathbf{T}\mathbf{n}\mathrm{d}l$;
      Find edge $e_{ij} = (s_i, v_j)$ with the largest $\mathbf{F}(s_i) \cdot \mathbf{e}_{ij}$;
      if $|\mathbf{F}(s_i)| > F_{ij}$ **then**
        Move singularity from s_i to v_j;
        $F_{ij} = |\mathbf{F}(s_i)|$
    end
    Compute φ using the singularities of θ;
  while !done;
  Compute $E_{\mathrm{smooth}}(\theta)$;
  if $E_{\mathrm{smooth}(\theta)} < E_{\min}$ **then**
    $k = 0$; $E_{\min} = E_{\mathrm{smooth}}(\theta)$; $\theta^* = \theta$;
  else
    $k++$;
end
Output θ^*;

Algorithm 2: Curl Elimination.

Data: A triangular mesh $M = (V, E, F)$ and a smooth cross field θ defined on triangular faces
Result: A smooth and integrable cross field θ
Computer the rotation vector ω of θ;
Compute $\mathbf{c} = \nabla\varphi - \mathbf{n} \times \omega$;
/* Reducing $\mathbf{c}$ via rotating θ */
$E_{\min} = \iint_M \|\mathbf{c}\|^2 \mathrm{d}\sigma$;
while true **do**
  Find the point p with the highest $\|\mathbf{c}\|$;
  Find a loop C containing p and having consistent sign $\mathbf{c} \cdot \mathrm{d}\mathbf{l}$;
  Solve Laplace's equation (18) to compute ψ;
  Rotate θ and ω by angle ψ;
  Update $\mathbf{c}$ with the rotated ω;
  Compute $E_{\mathbf{c}} = \iint_M \|\mathbf{c}^2\| \mathrm{d}\sigma$
  if $E_{\mathbf{c}} < E_{\min}$ **then**
    Save the current cross field θ; $E_{\min} = E_{\mathbf{c}}$;
  else
    Restore the previously saved θ; break;
end
/* Reducing $\mathbf{c}$ via moving singularities */
Compute φ using the singularities of θ;
Set $f_{\max}|_{e_{ij}} = 0$ for each edge $e_{ij} \in E$;
done = false;
while !done **do**
  done = true;
  for each singularity s_i **do**
    Set $\mathbf{f}_c(s_i) = 2\pi I(s_i)\mathbf{c}(s_i)$ for each singularity s_i;
    Find the singularity v_i with the largest force $\|\mathbf{f}_c\|$;
    Find the incident edge e_{ij} with the largest $|\mathbf{f}_{\mathbf{c}} \cdot \mathbf{f}_{\mathbf{c}}|$;
    Compute $f_{ij} = \frac{\mathbf{f}_{\mathbf{c}}(v_i) \cdot \overrightarrow{v_i v_j}}{\|\overrightarrow{v_i v_j}\|}$;
    if $|f_{ij}| > f_{\max}|_{e_{ij}}$ **then**
      $f_{max}|_{e_{ij}} = f_{ij}$;
      Move singularity from s_i to v_j;
      Update θ and ω;
      Compute φ with the same set of singularities of θ;
      Update $\mathbf{c} = \nabla\varphi - \mathbf{n} \times \omega$;
      done = false;
  end
end

mitigate the bias introduced by varying triangle sizes. Similarly, we have a compensation term in computing conformal factor φ at singularities. See the supplementary material for details. Second, in the discrete setting, unlike the continuous framework where singularities can move in any direction following $\mathbf{F}(s_i)$, movements are restricted to the mesh connectivity. Specifically, we confine singularities to mesh vertices and transition them from one vertex to another, moving them along mesh edges. This process involves identifying the edge e_{ij} that is incident to the singularity at vertex s_i and aligns most closely with $\mathbf{F}(s_i)$–the edge where the angle between $\mathbf{F}(s_i)$ and the edge direction is minimal. The singularity is then moved from s_i to the adjacent vertex v_j.

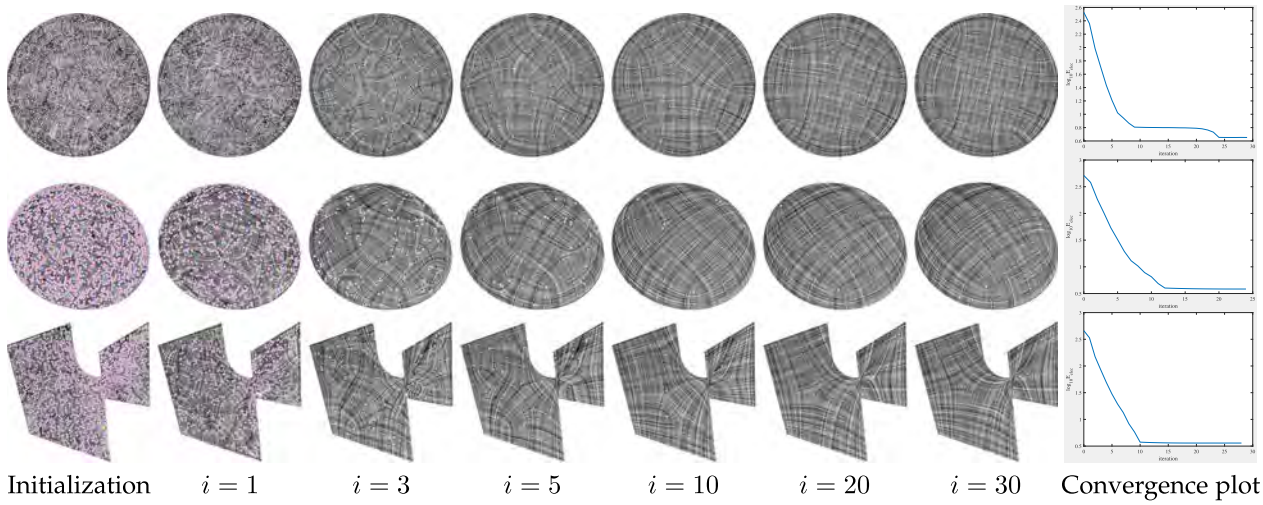

Fig. 13. In simple models where Gaussian curvatures exhibit consistent signs, local adjustments of singularities achieve globally optimal results.

VIII. Experimental Results

We implemented our algorithm in C++ and tested it on a PC equipped with an Inter(R) Xeon(R) E5-1650 CPU and 16 GB of RAM. The algorithm requires only a standard sparse linear solver to compute the conformal factor φ. For this purpose, we utilized Eigen,[2] which pre-factors the Laplacian matrix. Consequently, solving Poisson's (8) requires only linear time.

Given that our method iteratively moves singularities along mesh edges during both the smooth energy minimization and curl elimination processes, we operate on reasonably dense input meshes. These dense meshes provide ample degrees of freedom necessary for the adjustments of singularities. For models with lower resolution, we employ subdivision techniques to enhance the resolution (see Fig. 23). The test models used in our experiments ranged from 5K to 50K triangles. Our method is fairly efficient, typically taking less than 20 seconds per model.

Global conformal parameterization: To demonstrate the efficacy of our method, we applied it to compute global conformal parameterization. We processed the input mesh by cutting it into a topological disk, where the singularities of our computed cross field were positioned on the boundary. We then utilized the classic MIQ solver [4] to compute an integer-valued parameterization. Due to the integrability of our cross fields, the resulting conformal parameterizations closely matched our cross fields closely and were seamless across the cutting seams. We evaluated the quality of our conformal parameterizations using two commonly used metrics: shape distortion E_{SD} and area distortion E_{AD}. These metrics are from the first fundamental form of the parameterized surface. Specifically, E_{SD} is calculated based on the aspect ratio of an ellipse generated by the metric matrix of the parameterization, while E_{AD} is determined from the scalar stretch of local areas, quantifying how much the area is distorted in the parameterization process. Both metrics are designed such that a value of 1 indicates no distortion, with values greater than 1 indicating some level of distortion. Thus, values closer to 1 are indicative of higher quality conformal parameterizations.

Relation between disk radius r_0 and singularity configuration: The disk radius r_0 plays a critical role in controlling the number of singularities and the smoothness energy of the cross field. Note that we exclude the geodesic disks when computing the area integral for the smoothness energy E_{smooth}. As the radius increases, the integral domain decreases, leading to a reduction in the computed integral value. Consequently, this allows the addition of more singularities, each with a relatively small index, without a corresponding increase in the total smoothness energy. To standardize r_0 relative to the model size, we define it as $r_0 = 10^{-s}\sqrt{A}$, where A is the surface area of the model. We recommend setting the exponent s within the range $[1, 4]$. Fig. 14 illustrates the effects of varying disk radii on the parameterization of the Stanford Bunny. We observe that the number of singularities is roughly positively correlated with r_0. The minor fluctuations in Fig. 14 (right) are due to the trial-and-error method employed in the global pairing process (detailed in Section VI-A2).

Local injectivity is a highly desired characteristic in parameterization methods. Although our method lacks a theoretical guarantee for local injectivity, practical evaluations using the 8i Voxelized Full Bodies (8iVFB) dataset[3] demonstrate that it consistently upholds this property. Fig. 16 (rightmost) provides a typical example of a model from this dataset that has been parameterized by our method, illustrating its capability to maintain local injectivity.

Boundary alignment: Our method supports boundary alignment by incorporating boundary curves as the Dirichlet boundary condition in the computation of cross fields (3). As a result, the field lines align well with the boundaries, as illustrated in Fig. 17. This feature is particularly valuable in free-form architecture design, where precise boundary alignment is crucial, as shown in Fig. 22. However, this method can lead to significant area distortions, particularly when the boundaries include non-orthogonal corners, as illustrated in Fig. 18.

[2] http://eigen.tuxfamily.org/
[3] http://plenodb.jpeg.org/pc/8ilabs

$(3.4, 24, 1.527)$ $(3.0, 28, 1.120)$ $(2.7, 32, 1.053)$ $(2.5, 34, 1.035)$ $(2.3, 38, 1.089)$ $(2.1, 40, 1.051)$ $(1.7, 42, 1.050)$

Fig. 14. Controlling area distortions through disk radius r_0. A larger radius results in the generation of more singularities, which typically reduces area distortion in the parameterization. Each image below is annotated with a 3-tuple indicating $-\log_{10} r_0$, the number of singularities $|S|$, and the area distortion metric E_{AD}. The right-most figure provides plots of r_0 against E_{AD} and r_0 against $|S|$, visually demonstrating how changes in the disk radius impact both the area distortion and the count of singularities.

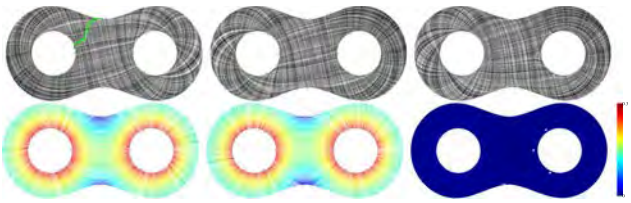

(a) $E_{\mathbf{c}} = 0.266$ (b) $E_{\mathbf{c}} = 0.257$ (c) $E_{\mathbf{c}} = 1.182 \times 10^{-4}$

Fig. 15. Discrete and continuous adjustments for curl elimination. (a) A smooth cross field initially exhibits significant curls. (b) Following discrete adjustment of θ, curls are reduced, though not completely eliminated. (c) Further fine-tuning of the locations of singularities diminishes $\mathbf{c}$ to a very low level, rendering θ effectively integrable.

Directional constraints are highly desired in the design of cross fields and in achieving conformal parameterization. Typically, adding constraints introduces curls in the cross field, making it non-integrable (see Fig. 19). Fortunately, curls in cross fields can be eliminated when a sufficient number of singularities are present (see Fig. 20). Our method allows users to specify *sparse hard* directional constraints in a trial-and-error manner (as illustrated in Fig. 27). We have observed that sparse constraints are effective in producing geometry-aware cross fields for simple shapes. For example, a single constraint applied to the base of the Greek Sculpture model (see Fig. 16, second from right) results in an optimal configuration, with eight singularities located at the base corners. Similarly, by placing two constraints on each finger of the Hand model, we achieved cross fields that are well aligned with the fingers' cylindrical geometry.

Sharp features: Our method can handle sharp features by allowing users to specify directional constraints along sharp edges. Fig. 28 shows the Fandisk model, where 102 constraints were applied. The resulting cross fields and conformal parameterization align well with most of the sharp features.

Extension: Our method can be extended to compute N-RoSy fields for any $N \in \mathbb{Z}_+$, where the field index $I(s_i)$ is a multiple of $\frac{1}{N}$. Equations (8) (2) and (6) for computing φ and θ, and the algorithms for minimizing the potential energy and eliminating curls remain unchanged. This is because their functionality does not rely on a specific value of N. Fig. 21 demonstrates the application of our method to a 6-Rosy field and the resulting isotropic triangle mesh.

Comparison with Ben-Chen et al.'s method [25]: While both our method and that of Ben-Chen et al. employ heuristics based on the conformal factor difference between point pairs, the underlying strategies and outcomes of the two approaches are fundamentally different. First, their method begins with a singularity-free configuration and iteratively introduces new singularities at points exhibiting the largest conformal factor differences. This process continues until the conformal factor difference falls below a specified threshold. In contrast, our method starts from a random cross field typically rich in singularities, and adjusts these by moving them along the gradient of conformal factor. To avoid getting stuck at local optimal, we force the points with the largest conformal difference towards each other, effectively reducing the total number of singularities. Second, their strategy is based on the intuition that points with extreme conformal factors make good candidates for singularities. Our strategy, alternatively, focuses on annihilating pair of points with the largest potential differences, thereby reducing the peak-to-valley range of φ, which is likely to reduce the Dirichlet energy and smooth the field (as illustrated in Figs. 9 and 14). Third, our method provides control over the number of singularities by adjusting the parameter r_0 (see Fig. 14), whereas their method regulates singularity counts by setting a threshold for the conformal factor difference. Fourth, our method aims at computing integrable cross fields, leading to seamless parameterizations. Their method scales the metric using the conformal factor to compute a 2D embedding, resulting in parameterizations with seams. Fifth, our method supports sparse hard directional constraints and aligns closely with boundaries, enhancing its applicability in practical scenarios. Ben-Chen et al.'s method does not offer similar capabilities for handling directional constraints or boundary alignment.

Comparison with the GL-functional [33]: While Ginzburg-Landau (GL) theory offers a sound and elegant framework for computing boundary-aligned cross fields, it does not support directional constraints nor does it guarantee integrability. Furthermore, Viertel and Osting [33] limited their demonstrations to planar cases, and to date, there has been no documented implementation of GL theory on curved surfaces in existing literature. Our method, in contrast, supports sparse directional constraints, and allows users to control the number of singularities, and guarantees integrability. Moreover, our method works for both planar domains and curved surfaces of arbitrary topology, since the singularity operations (e.g., movement, merging and split)

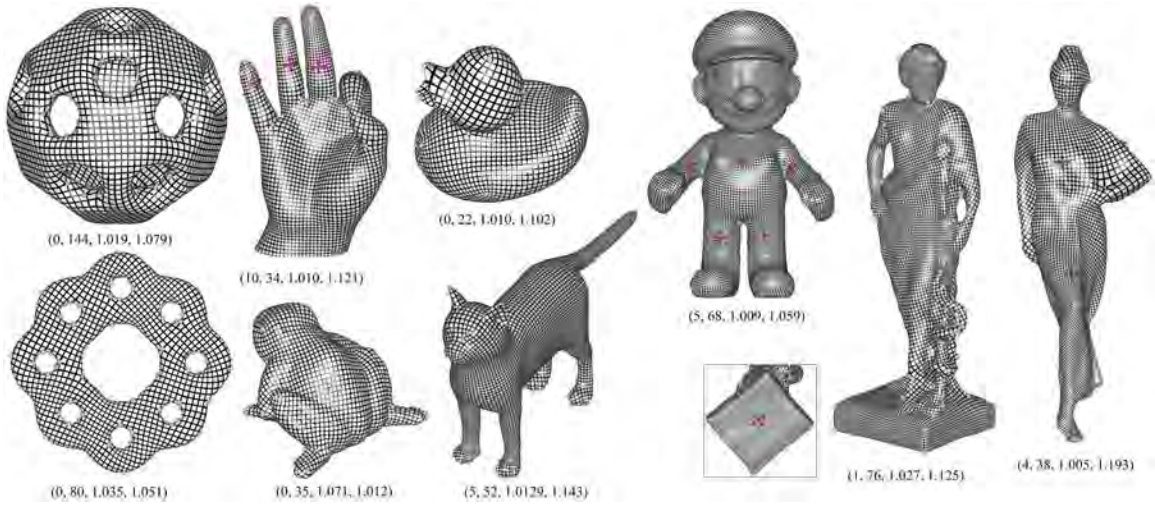

Fig. 16. Seamless conformal parameterization induced by our cross fields. Our method works well for smooth surfaces with or without boundaries. Each image includes a 4-tuple annotation detailing the number of directional constraints $|C|$, the number of singularities N_s, the angle distortion E_{SD}, and the area distortion E_{AD}. Images are rendered in high-resolution to facilitate detailed examination upon zooming.

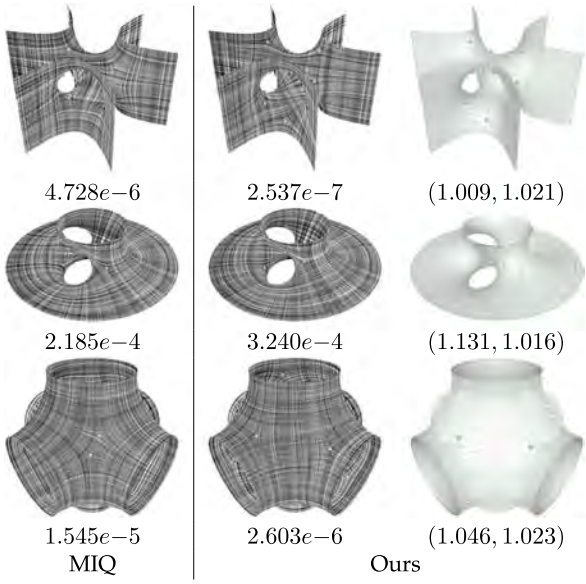

Fig. 17. Models with boundaries. The parameter lines are well aligned with the boundaries, and the locations of the singularities also roughly capture the global and local symmetries of the input surfaces, without the addition of directional constraints. Below each cross field, the displayed value represent the smoothness energy, while the 2-tuple accompanying the quad meshes details the angle and area distortions, respectively.

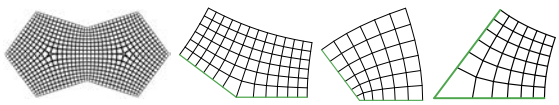

Fig. 18. Given that crosses are orthogonal to the boundary curves, non-orthogonal corners typically induce significant area distortions.

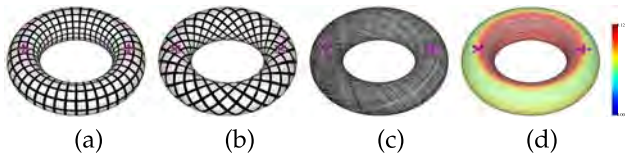

Fig. 19. Compatible and incompatible directional constraints. (a) and (b) show two examples of conformal seamless parameterization with compatible constraints. (c) shows a pair of incompatible constraints, leading to a cross field that is not integrable. (d) shows the vector field $\mathbf{c} \neq \mathbf{0}$, highlighting the presence of discrepancies due to the incompatible constraints.

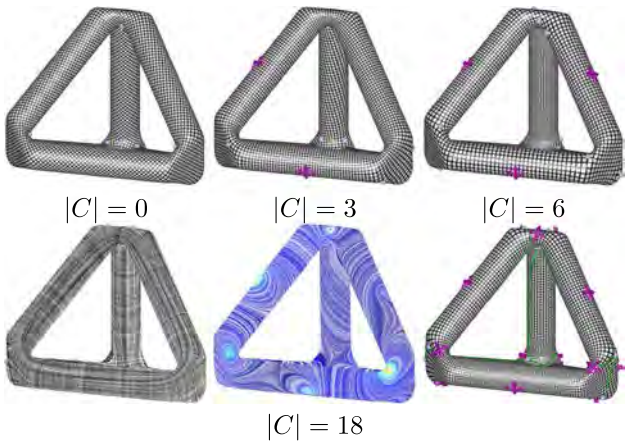

Fig. 20. Our method allows sparse hard directional constraints. The first row shows a toy model with 0, 3 and 6 constraints, respectively. We observe that 6 constraints are sufficient to yield high-quality, geometry-aware parameterization. The second row shows a cross field with 18 constraints. Although still smooth, it is no longer integrable, as evidenced by the non-vanishing discrepancy field $\mathbf{c}$. Consequently, the model had to be segmented into a topological disk to compute a conformal parameterization with seam (green curves).

are local and our method does not require a global coordinate system. Moreover, in [33], the GL-functional is computed over the entire domain including singularities. In contrast, our method removes singularities and their vicinities to obtain tessellation independent energy. As a by-product, our method allows the user to tune the radius of the geodesic disk to balance the smoothness energy and the number of singularities, whereas their method cannot control the number of singularities.

Comparison with IOQ [12]: First, IOQ is theoretically sound and has an elegant formulation based on the resistance distance

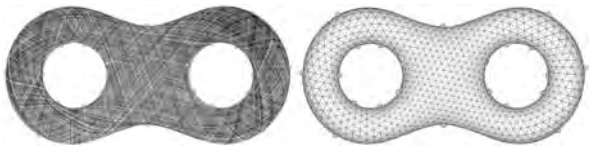

Fig. 21. Our method can be extended to compute smooth N-RoSy fields for various values of N. Illustrated here is a 6-RoSy field applied to a two-holed torus, featuring 16 valence-7 and 6 valence-5 vertices, while all other vertices maintain regular valence of 6.

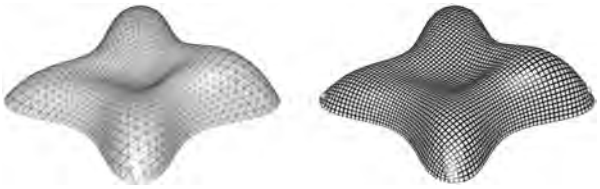

Fig. 22. Applying our method to architectural geometry can yield high-quality quadrilateral meshes, which provide more aesthetic value than triangle meshes. This example has 4 singularities and low angle and area distortions $E_{SD} = 1.009$ and $E_{AD} = 1.033$. Thanks to our boundary alignment feature, the parameter lines are well aligned with the surface boundary.

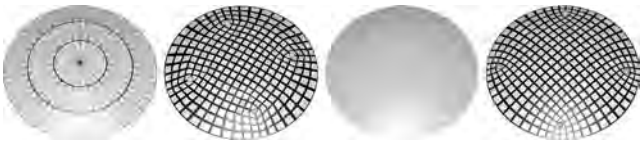

Fig. 23. Our method necessitates a triangle mesh of relatively high resolution to adequately provide the necessary degrees of freedom for singularity placement. Row 1: Given a triangle mesh with a high degree of anisotropy and low resolution, the singularities are constrained to the mesh vertices, leading to large angle and area distortions in the resulting parameterization. Row 2: Increasing the mesh resolution can reduce these distortions.

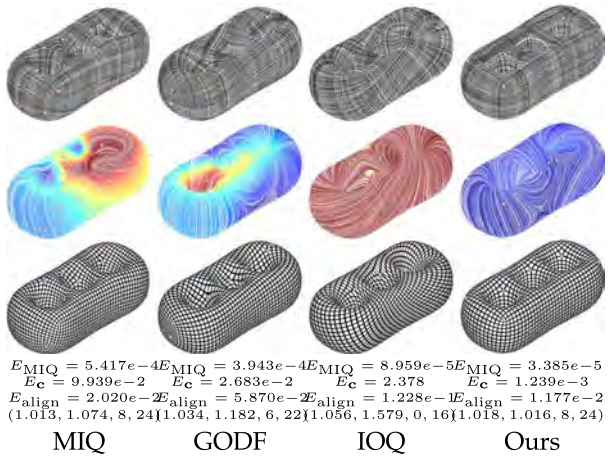

Fig. 24. Thanks to integrability, our parameterization is well aligned with the cross field. We observe misalignment in the results of MIQ, GODF and IOQ, which are not integrable. E_{align} is the alignment measure. The 4-tuple is E_{AD}, E_{SD}, the number of position and negative singularities, respectively.

Fig. 25. The optimal cone singularity method [31] can produce very few singularities and low distortions. However, their parameterization is not seamless.

matrix. Our method is loosely based on a physics model that drives singularities to optimal locations. Second, their method can be easily parallelized on GPUs, but is still computationally expensive. For example, their approximate algorithm takes around 20 seconds for a mesh with 50 K faces on an Intel Core i7 CPU and an NVIDIA GTX 1080 Ti GPU, while our method takes no more than 3 seconds on the CPU only. Third, IOQ does not guarantee integrability and cannot support directional constraints or boundary alignment, while our method can. Fourth, IOQ is numerically stable and can tolerate geometric noise of certain degree, while our method requires the input meshes are smooth and free of noise. Fifth, for most of the test models, IOQ produces fewer singularities than ours. However, we observed that on high-genus models, their results often have larger area and angle distortions than ours (see Fig. 24).

Comparison with other field methods: Table I list the major directional field methods with features. We quantitatively compare our method with 5 representative directional field methods: mixed integer quadrangulation (MIQ) [4], globally optimal direction field (GODF) [11], integer-only cross field (IOQ) [12], frame field (FF) [20], and integrable polyvector field (IPF) [13].

Note that MIQ, GODF and IOQ are cross fields, and FF and IPF are non-orthogonal fields. A major application of cross field is to guide a global parameterization. Our results with and without curl elimination share the same number of singularities and indices. Optimizing their locations can eliminate curls and make the cross field integrable.

Thanks to integrability, our parameterizations are well aligned with the cross fields for all test models. To quantitatively measure the alignment, we define the following metric

$$E_{\text{align}} = \iint (h\nabla u - \mathbf{e}_u)^2 + (h\nabla v - \mathbf{e}_v)^2 \mathrm{d}\sigma,$$

where $(\mathbf{e}_u, \mathbf{e}_v)$ are the cross directions and h is the global scale factor [4]. In Fig. 24, we compare our method with the other cross field methods in terms of integrability. We observe that the alignment measures of our results are consistently better than the other cross field methods.

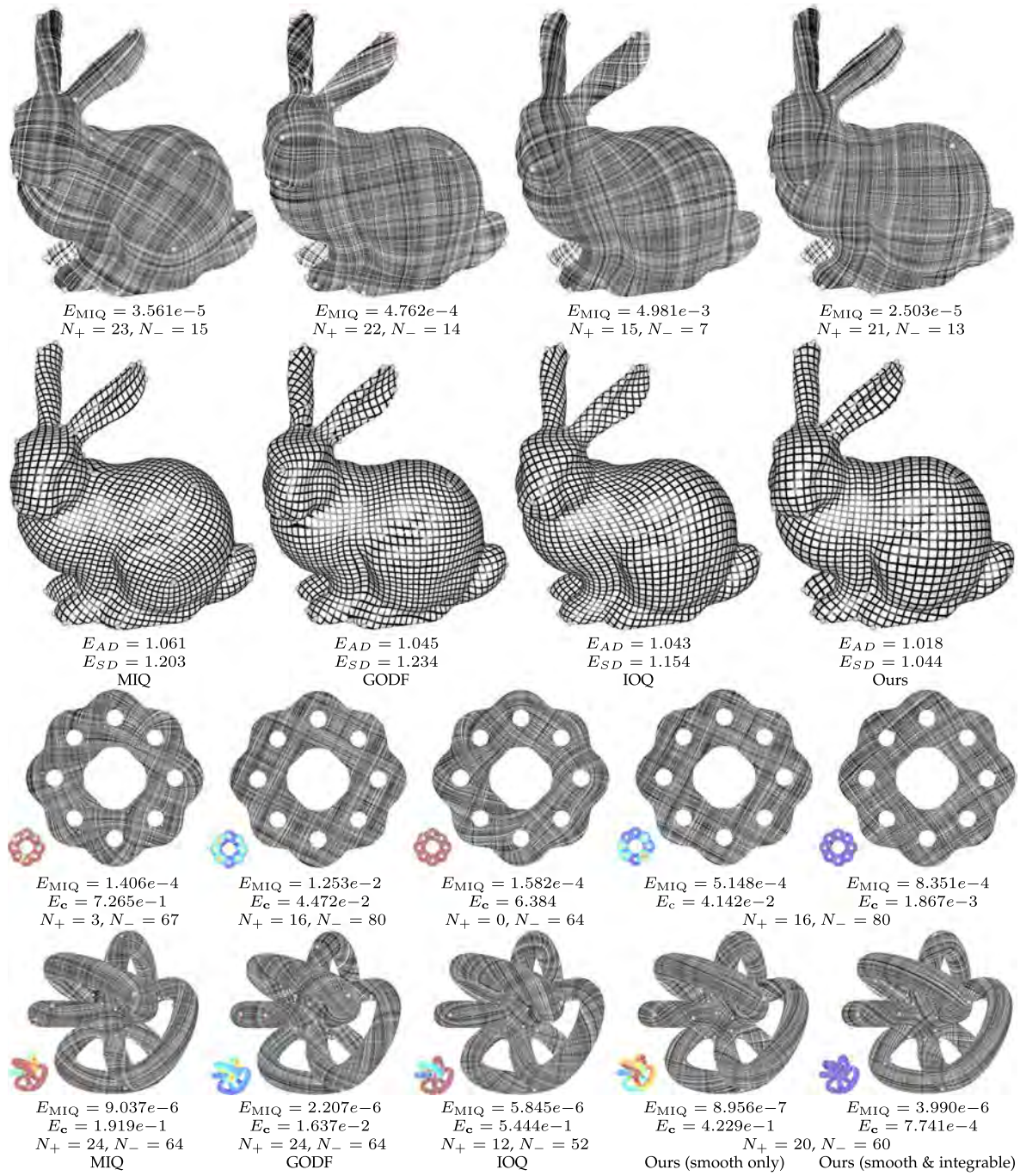

Fig. 26. Comparing to other cross field methods, including MIQ [4], GODF [11] and IOQ [12]. For simply connected domains, smooth cross fields are also integrable. But for multiply connected domains, only our method can produce integrable cross fields. The small insets show the vector field $\mathbf{c}$. E_{MIQ} is the MIQ energy [4] for measuring the smoothness of cross fields (without removing the singularities). $E_{\mathbf{c}}$ measures how far the cross field is from an integrable field. N_+ and N_- are the number of singularities with indices $\frac{1}{4}$ and $\frac{-1}{4}$, respectively.

IPF can also compute integrable fields, but their fields are non-orthogonal. As a result, their induced parameterizations have larger angle distortions than ours. Since PolyVector fields have larger solution space than cross fields, IPF allows the user to specify more soft constraints in an intuitive manner (e.g., by simple sketches on the model). Our method, which is restricted to cross fields, can only take sparse hard constraints in a trial-and-error manner. GODF supports soft directional constraints, and MIQ supports both hard and soft directional constraints. IOQ does not support directional constraints nor boundary alignment.

We observe that IOQ produces the fewest singularities for most of the test models. For the simple toy model (Fig. 27, row 1), our method generates more singularities than other approaches. These singularities are well-placed, faithfully capturing both global and local symmetry. For models with non-trivial topology,

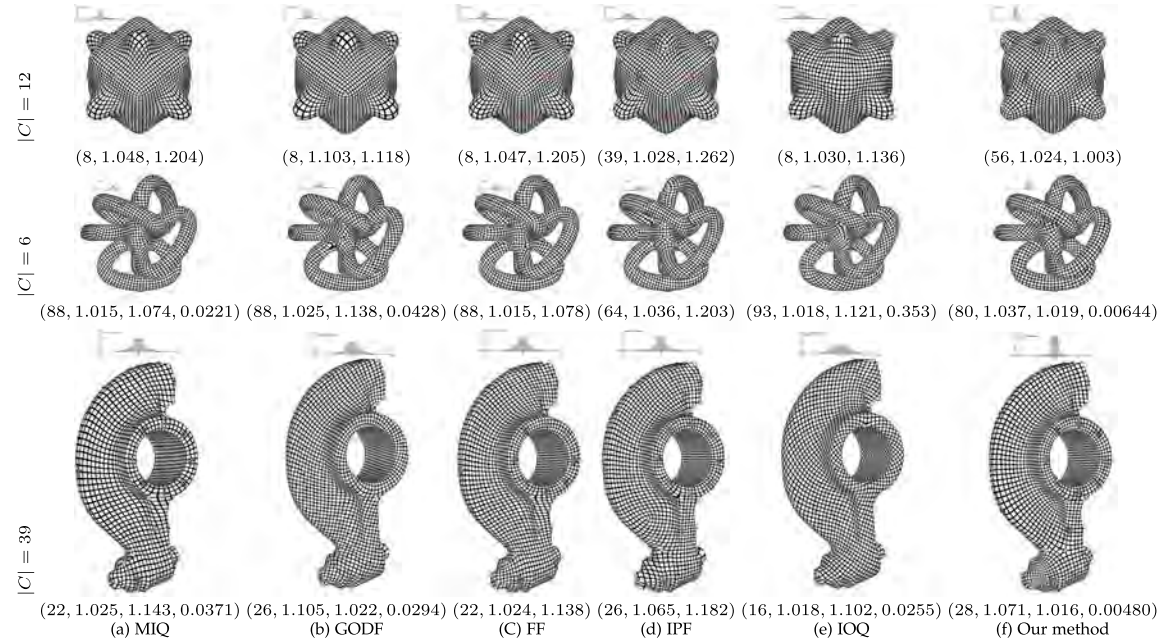

Fig. 27. Comparison. The positive and negative singularities are colored in pink and cyan, respectively. The pink crosses are the **hard** directional constraints. $|C|$ is the number of constraints. The numbers below each figure are the number of singularities $|S|$, area distortion E_{AD}, and angle distortion E_{SD}. For cross field methods (i.e., MIQ, GODF, IOQ and ours), the last number is the alignment measure E_{align}. The histograms show the angle distribution. The images are rendered in high resolution, allowing zoom-in examination. Note that GODF supports soft constraints and IOQ does not support directional constraints.

TABLE I
QUALITATIVE COMPARISON OF REPRESENTATIVE CROSS AND DIRECTIONAL FIELD METHODS

Method	Domain	Orthogonal	Efficiency	Boundary alignment	Directional constraints	Dirichlet energy	Integrability	Singularity number	Sharp features
MIQ [4]	3D	Yes	Fair	Yes	Dense, hard/soft	Low	No	Fair	Yes
GODF [11]	3D	Yes	Fast	No	Dense, hard/soft	Low	No	Fair	Yes
FF [20]	3D	No	Fair	Yes	Dense, hard	Low	No	Fair	Yes
IPF [13]	3D	No	Fair	Yes	Dense, hard/soft	Fair	Yes	Fair	Yes
IOQ [12]	3D	Yes	Fair	No	No	Low	No	Small	No
m-harmonic [18]	3D	Yes	Fast	Yes	Dense, hard/soft	Low	No	Fair	No
GL-functional [34]	2D	Yes	Fast	Yes	No	Low	No	Fair	No
OF [19]	3D	Yes	Fair	Yes	Dense, soft	Fair	No	Fair	Yes
Chebshev Net [24]	3D	No	Fair	Yes	No	Low	Yes	Small	Yes
Metric Customization [21]	3D	No	Fair	Yes	Dense hard/soft	Fair	No	Fair	Yes
Ours	3D	Yes	Fair	Yes	Sparse, hard	Low	Yes	Fair	Fair

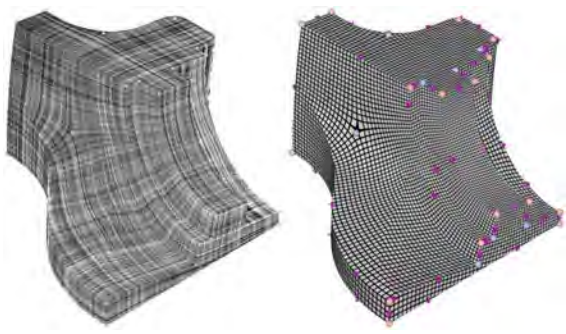

Fig. 28. Our method can partially support sharp features by specifying sparse hard directional constraints. $|C| = 102$, $N_+ = 20$, $N_- = 12$, $E_{AD} = 1.01521$, $E_{SD} = 1.06955$.

our method yields a comparable number of singularities to other methods (see Fig. 27, rows 2 and 3, and Fig. 24).

We also compare our method with [31] that computes conformal parameterization with optimal cone singularity and minimal area distortion (MAD). As a convex optimization, MAD is numerically robust and efficient, and yields results with a small number of singularities and a small total cone angles. However, MAD does not support directional constraints and boundary alignment and its produced parameterizations have seams. See Fig. 25.

By specifying sparse hard constraints, our method can partially support sharp features. The metric customization method [21] is flexible to support both sparse and dense constraints, and also works well for sharp features. However, the cost is lack of orthogonality. The octahedral frame method [19] minimizes energies with *soft* normal alignment constraints, therefore, it is able to fully support sharp features and compute feature-aligned cross fields. The Chebyshev Net method [15] addresses integrability by adding a soft constraint in the GL-functional, and it also allows boundary alignment constraints and supports sharp features. However, it produces polyvector fields, which in general are not orthogonal.

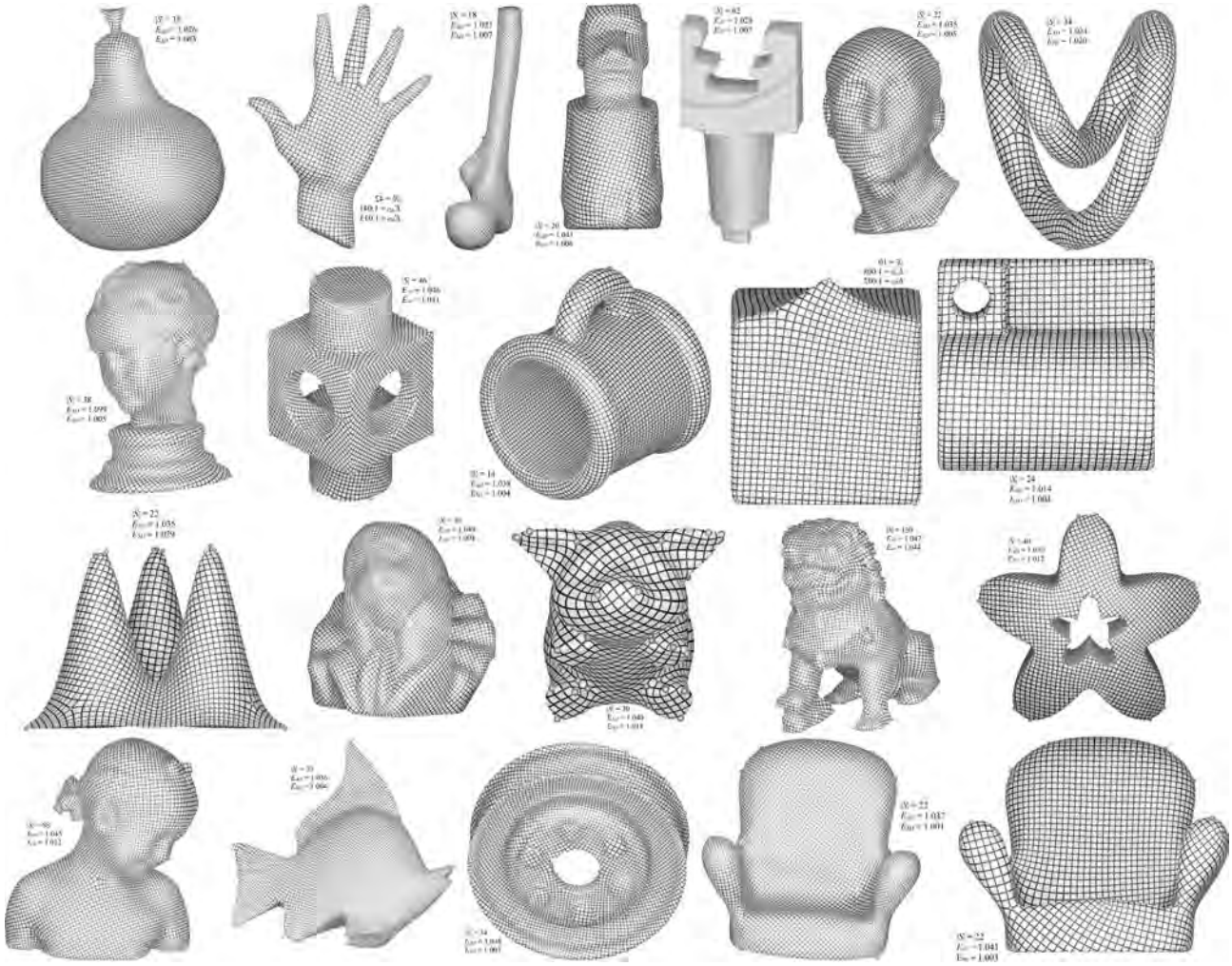

Fig. 29. Additional results on seamless conformal parameterization. For each model, we show the number of singularities and the area and angle distortions.

IX. Conclusion

In the paper, we investigate the integrability problem of cross fields on surfaces of arbitrary topology. A cross field is smooth if it has a locally minimal Dirichlet energy. However, unless the surface is simply connected, a smooth cross field is not necessarily integrable. We prove that a smooth cross field is integrable if $\mathbf{c} \equiv \mathbf{0}$ holds everywhere. Based on the theoretical results, we develop a novel method for computing smooth and integrable cross fields on 3D surfaces of complex topology. Our method is fully automatic and also has a parameter that can balance the number of singularities and the smoothness energy. The proposed method is well suited for smooth models in which exact boundary alignment and sparse hard directional constraints are desired, and can guide seamless conformal parameterization (see Fig. 29) and T-junction-free quadrangulation.

Acknowledgment

The authors would like to thank the anonymous reviewers for their valuable feedback. A significant portion of the work was conducted while the first author was a Research Fellow at NTU.

References

[1] J. Palacios and E. Zhang, "Rotational symmetry field design on surfaces," *ACM Trans. Graph.*, vol. 26, no. 3, pp. 55–es, 2007.
[2] N. Ray, B. Vallet, W. Li, and B. Lévy, "N-symmetry direction field design," *ACM Trans. Graph.*, vol. 27, no. 2, pp. 10:1–10:13, 2008.
[3] A. Hertzmann and D. Zorin, "Illustrating smooth surfaces," in *Proc. 27th Annu. Conf. Comput. Graph. Interactive Techn.*, 2000, pp. 517–526.
[4] D. Bommes, H. Zimmer, and L. Kobbelt, "Mixed-integer quadrangulation," *ACM Trans. Graph.*, vol. 28, no. 3, pp. 1–10, 2009.
[5] W. Jakob, M. Tarini, D. Panozzo, and O. Sorkine-Hornung, "Instant field-aligned meshes," *ACM Trans. Graph.*, vol. 34, no. 6, pp. 189:1–189:15, 2015.
[6] X. Liang, M. S. Ebeida, and Y. Zhang, "Guaranteed-quality all-quadrilateral mesh generation with feature preservation," *Comput. Methods Appl. Mechanics Eng.*, vol. 199, no. 29, pp. 2072–2083, 2010.
[7] G. Xu, M. Li, B. Mourrain, T. Rabczuk, J. Xu, and S. P. Bordas, "Constructing iga-suitable planar parameterization from complex cad boundary by domain partition and global/local optimization," *Comput. Methods Appl. Mechanics Eng.*, vol. 328, pp. 175–200, 2018.
[8] K. Crane, M. Desbrun, and P. Schröder, "Trivial connections on discrete surfaces," *Comput. Graph. Forum*, vol. 29, no. 5, pp. 1525–1533, 2010.
[9] F. Kälberer, M. Nieser, and K. Polthier, "Quadcover - surface parameterization using branched coverings," *Comput. Graph. Forum*, vol. 26, no. 3, pp. 375–384, 2007.
[10] D. Bommes, M. Campen, H. Ebke, P. Alliez, and L. Kobbelt, "Integer-grid maps for reliable quad meshing," *ACM Trans. Graph.*, vol. 32, no. 4, pp. 98:1–98:12, 2013.

[11] F. Knöppel, K. Crane, U. Pinkall, and P. Schröder, "Globally optimal direction fields," *ACM Trans. Graph.*, vol. 32, no. 4, pp. 59:1–59:10, 2013.
[12] N. Farchi and M. Ben-Chen, "Integer-only cross field computation," *ACM Trans. Graph.*, vol. 37, no. 4, 2018, Art. no. 91.
[13] O. Diamanti, A. Vaxman, D. Panozzo, and O. Sorkine-Hornung, "Integrable polyvector fields," *ACM Trans. Graph.*, vol. 34, no. 4, 2015, Art. no. 38.
[14] G. Bunin, "A continuum theory for unstructured mesh generation in two dimensions," *Comput. Aided Geometric Des.*, vol. 25, no. 1, pp. 14–40, 2008.
[15] A. O. Sageman-Furnas, A. Chern, M. Ben-Chen, and A. Vaxman, "Chebyshev nets from commuting polyvector fields," *ACM Trans. Graph.*, vol. 38, no. 6, pp. 172:1–172:16, Nov. 2019.
[16] N. Ray, W. Li, B. Lévy, A. Sheffer, and P. Alliez, "Periodic global parameterization," *ACM Trans. Graph.*, vol. 25, no. 4, pp. 1460–1485, 2006.
[17] A. Vaxman et al., "Directional field synthesis, design, and processing," *Comput. Graph. Forum*, vol. 35, no. 2, pp. 545–572, 2016.
[18] C. Brandt, L. Scandolo, E. Eisemann, and K. Hildebrandt, "Modeling n-symmetry vector fields using higher-order energies," *ACM Trans. Graph.*, vol. 37, no. 2, pp. 18:1–18:18, 2018.
[19] P. Zhang, J. Vekhter, E. Chien, D. Bommes, E. Vouga, and J. Solomon, "Octahedral frames for feature-aligned cross fields," *ACM Trans. Graph.*, vol. 39, no. 3, pp. 25:1–25:13, 2020.
[20] D. Panozzo, E. Puppo, M. Tarini, and O. Sorkine-Hornung, "Frame fields: Anisotropic and non-orthogonal cross fields," *ACM Trans. Graph.*, vol. 33, no. 4, pp. 134:1–134:11, 2014.
[21] T. Jiang, X. Fang, J. Huang, H. Bao, Y. Tong, and M. Desbrun, "Frame field generation through metric customization," *ACM Trans. Graph.*, vol. 34, no. 4, pp. 40:1–40:11, Jul. 2015.
[22] O. Gutan, S. Hegde, E. Berumen, M. Bessmeltsev, and E. Chien, "Singularity–free frame fields for line drawing vectorization," *Comput. Graph. Forum*, vol. 42, no. 5, pp. i–viii, 2023.
[23] O. Diamanti, A. Vaxman, D. Panozzo, and O. Sorkine-Hornung, "Designing n-PolyVector fields with complex polynomials," *Comput. Graph. Forum*, vol. 33, no. 5, pp. 1–11, 2014.
[24] H. Shen, L. Zhu, R. Capouellez, D. Panozzo, M. Campen, and D. Zorin, "Which cross fields can be quadrangulated?: Global parameterization from prescribed holonomy signatures," *ACM Trans. Graph.*, vol. 41, pp. 1–12, 2022.
[25] M. Ben-Chen, C. Gotsman, and G. Bunin, "Conformal flattening by curvature prescription and metric scaling," *Comput. Graph. Forum*, vol. 27, no. 2, pp. 449–458, 2008.
[26] B. Springborn, P. Schröder, and U. Pinkall, "Conformal equivalence of triangle meshes," *ACM Trans. Graph.*, vol. 27, no. 3, pp. 1–11, 2008.
[27] A. Myles and D. Zorin, "Global parametrization by incremental flattening," *ACM Trans. Graph.*, vol. 31, no. 4, pp. 109:1–109:11, Jul. 2012.
[28] A. Myles and D. Zorin, "Controlled-distortion constrained global parametrization," *ACM Trans. Graph.*, vol. 32, no. 4, pp. 105:1–105:14, Jul. 2013.
[29] A. Bright, E. Chien, and O. Weber, "Harmonic global parametrization with rational holonomy," *ACM Trans. Graph.*, vol. 36, no. 4, 2017, Art. no. 89.
[30] M. Campen and D. Zorin, "Similarity maps and field-guided T-splines: A perfect couple," *ACM Trans. Graph.*, vol. 36, no. 4, pp. 91:1–91:16, 2017.
[31] Y. Soliman, D. Slepčev, and K. Crane, "Optimal cone singularities for conformal flattening," *ACM Trans. Graph.*, vol. 37, no. 4, 2018, Art. no. 105.
[32] M. Campen, H. Shen, J. Zhou, and D. Zorin, "Seamless parametrization with arbitrary cones for arbitrary genus," *ACM Trans. Graph.*, vol. 39, no. 1, pp. 2:1–2:19, 2020.
[33] R. Viertel and B. Osting, "An approach to quad meshing based on harmonic cross-valued maps and the ginzburg-landau theory," *SIAM J. Sci. Comput.*, vol. 41, no. 1, pp. A452–A479, 2017.

Long Ma received the PhD degree from the School of Computer Science and Technology, Shandong University, in 2017. He is an associate researcher with the School of Software, Shandong University. His research focuses on computer graphics, geometry modeling, and mechanical simulation.

Ying He (Member, IEEE) is an associate professor with the College of Computing and Data Science and serves as the director of the Centre for Augmented and Virtual Reality, Nanyang Technological University, Singapore. His research primarily focuses on geometric computing and analysis. He is an active member of the technical program committees of major conferences in geometric modeling and has held positions on the editorial boards of leading journals, including *IEEE Transactions on Visualization and Computer Graphics*, *Computer Graphics Forum*, and *Computational Visual Media*. His leadership roles have included General or program co-chair for several prominent conferences, such as the Shape Modeling International Conference (2022), the Symposium on Solid and Physical Modeling (2022 and 2023), the Geometric Modeling and Processing Conference (2014 and 2021), and the Conference on Computational Visual Media (2020).

Jianmin Zheng received the PhD degree from Zhejiang University, China. He is a professor with the School of Computer Science and Engineering, Nanyang Technological University, Singapore. His recent research interests include digital geometric processing, reality computing, and AI assisted part design for 3D printing. He is currently the programme director for the research pillar of ML/AI under the HP-NTU Digital Manufacturing Corporate Lab. He is also a member of executive committee of the Asia Graphics Association.

Yuanfeng Zhou received the PhD degree from the School of Computer Science and Technology, Shandong University, in 2009. He is currently a professor with the School of Software, Shandong University, where he is also a member of the IGIP Laboratory. His current research interests include geometric modeling, information visualization, and image processing. He held a post-doctoral position with the Graphics Group, Department of Computer Science, The University of Hong Kong, Hong Kong, from 2009 to 2011.

Shiqing Xin received the PhD degree in applied mathematics from Zhejiang University. He is an associate professor with the School of Computer Science and Technology, Shandong University. His research focuses on geometric calculation, geometric modeling, and scene understanding.

Caiming Zhang received the BS and ME degrees in computer science from the Shandong University, in 1982 and 1984, respectively, and the DrEng degree in computer science from the Tokyo Institute of Technology, Japan, in 1994. He is a professor and doctoral supervisor with the School of Computer Science and Technology, Shandong University. From 1997 to 2000, he has held visiting position at the University of Kentucky, USA. His research interests include CAGD, CG, information visualization and medical image processing.

Wenping Wang (Fellow, IEEE) received the PhD degree in computer science from the University of Alberta, in 1992. He is currently a chair professor of computer science with the University of Hong Kong. His research interests include computer graphics, computer visualization, computer vision, robotics, medical image processing, and geometric computing. He is associate editor of several premium journals, including the *Computer Aided Geometric Design* (CAGD), *Computer Graphics Forum* (CGF), *IEEE Transactions on Computers*, and *IEEE Computer Graphics and Applications*, and has chaired more than 20 international conferences, including Pacific Graphics 2012, ACM Symposium on Physical and Solid Modeling (SPM) 2013, SIGGRAPH Asia 2013, and Geometry Submit 2019. He received the John Gregory Memorial Award for his contributions in geometric modeling.